Mon. Not. R. Astron. Soc. **000**, 1–24 (2012) Printed 18 April 2012 (MN LATEX style file v2.2)

The VLT LBG Redshift Survey - III. The clustering and dynamics of Lyman-break galaxies at $z \sim 3$ ⋆

R. Bielby[1]†, M. D. Hill[1], T. Shanks[1], N. H. M. Crighton[1,2], L. Infante[3], C. G. Bornancini[4], H. Francke[3], P. Héraudeau[5,6], D. G. Lambas[4], N. Metcalfe[1] D. Minniti[3,7,8], N. Padilla[3], T. Theuns[9,10], P. Tummuangpak[1], P. Weilbacher[11]

[1] *Durham University, South Road, Durham, DH1 3LE, United Kingdom*
[2] *Max Planck Institute for Astronomy, Knigstuhl 17, D-69117 Heidelberg, Germany*
[3] *Departamento de Astronomía y Astrofísica, Pontificia Universidad Catolica de Chile, Casilla 306, Santiago 22, Chile*
[4] *Instituto de Astronomía Teórica y Experimental (CONICET-UNC), Observatorio Astronómico de Córdoba, Laprida 854, X5000BGR, Córdoba, Argentina*
[5] *Argelander Institut für Astronomie, Auf dem Hügel 71, 53121 Bonn, Germany*
[6] *Kapteyn Astronomical Institute, University of Groningen, PO Box 800, 9700 AV, Groningen, The Netherlands*
[7] *Vatican Observatory, V00120 Vatican City State, Italy*
[8] *Department of Astrophysical Sciences, Princeton University, Princeton NJ 08544-1001, USA*
[9] *Institute for Computational Cosmology, Department of Physics, University of Durham, South Road, Durham, DH1 3LE, UK*
[10] *Department of Physics, University of Antwerp, Campus Groenenborger, Groenenborgerlaan 171, B-2020 Antwerp, Belgium*
[11] *Leibniz-Institut für Astrophysik Potsdam (AIP), Germany*

First draft 2012 April 5

ABSTRACT

We present a survey of 2,148 galaxy redshifts from the VLT LBG Redshift Survey (VLRS), a spectroscopic survey of $z \approx 3$ galaxies in wide fields centred on background QSOs. We have used deep optical imaging to select these galaxies via the Lyman break technique. Spectroscopy of the Lyman Break Galaxies (LBGs) was then made using the VLT VIMOS instrument, giving a mean redshift of $z \approx 2.78$. To make a definitive LBG clustering analysis, we have combined the VLRS redshifts with the 813 Keck LBG redshifts of Steidel et al, with the statistical power of VLRS at large scales complementing the accuracy of the Keck sample at small scales. From the semi-projected correlation function, $w_p(\sigma)$, for the VLRS and combined surveys, we find that the results are well fit with a single power law model for the real space correlation function, $\xi(r)$, with clustering scale lengths of respectively $r_0 = 3.32 \pm 0.41$ and 3.75 ± 0.24 h^{-1}Mpc. *We note that the corresponding combined $\xi(r)$ slope is flatter than for local galaxies at $\gamma = 1.55 \pm 0.09$ rather than $\gamma = 1.8$. This flat slope is confirmed by the z-space correlation function, $\xi(s)$, and in the range* $10 < s < 100$ h^{-1}Mpc *the VLRS shows an $\approx 2.5\sigma$ excess over the ΛCDM linear prediction.* This excess may be consistent with recent evidence for non-Gaussianity in clustering results at $z \approx 1$. We then analyse the LBG z-space distortions using the 2-D correlation function, $\xi(\sigma, \pi)$, finding for the combined sample a large scale infall parameter of $\beta = 0.32 \pm 0.20$ and a velocity dispersion of $\sqrt{\langle w_z^2 \rangle} = 540^{+180}_{-200}$kms^{-1}. Fixing this velocity dispersion, we fit $\xi(\sigma, \pi)$ for Ω_m and β and break their degeneracy using low-z data to find $\Omega_m(z = 0) = 0.30^{+0.32}_{-0.18}$. Finally, based on our measured β, we are able to determine the gravitational growth rate, finding a value of $f(z = 3) = 0.83 \pm 0.46$ (or $f\sigma_8 = 0.22 \pm 0.12$), which is the highest redshift measurement of the growth rate via galaxy clustering and is consistent with Einstein gravity and ΛCDM.

Key words: galaxies: kinematics and dynamics - cosmology: observations - large-scale structure of Universe

⋆ Based on data obtained with the NOAO Mayall 4m Telescope at Kitt Peak National Observatory, USA (programme ID: 06A-

1 INTRODUCTION

The large scale structure of matter presents a crucial guide in understanding the nature and evolution of the Universe. In ΛCDM, structure in the Universe grows hierarchically through gravitational instability (e.g. Mo & White 1996; Jenkins et al. 1998; Springel et al. 2006) and testing this model requires the measurement of the matter clustering and the growth of structure across cosmic time (e.g. Springel et al. 2005; Orsi et al. 2008; Kim et al. 2009). We are limited however in our ability to trace the structure of mass given that the ΛCDM model suggests that ≈ 80% of the mass density of the Universe is in the form of dark matter.

Although large photometric surveys are beginning to map the overall matter density distribution via its lensing signature (e.g. Massey et al. 2007; Hildebrandt et al. 2012), at present the key tool in the statistical analysis of the distribution of matter in the Universe remains the study of the clustering statistics of selected galaxy populations. A given galaxy population traces the peaks in the matter distribution and hence provides a biased view of the matter density, which nevertheless can be used to follow the overall growth of structure.

At low-redshift, magnitude limited galaxy samples have provided significant tools in probing the clustering properties of the galaxy population (e.g. Norberg et al. 2002; Hawkins et al. 2003). Moving to higher redshifts, photometric selections are required to isolate the required redshift range, for example the Luminous Red Galaxy (LRG), Emission Line Galaxy (ELG), BzK, Extremeley Red Object (ERO), Distant Red Galaxy (DRG) selections. At $z > 2$, identifying galaxy populations is primarily reliant on the Lyman Break (e.g. Steidel et al. 1996, 1999, 2003; Adelberger et al. 2003; Franx et al. 2003) and the Ly-α emitter (LAEs; e.g. Cowie & Hu 1998; Gawiser et al. 2006, 2007; Ouchi et al. 2008) selections.

Lyman break galaxies (LBGs) facilitated for the first time observational estimates of the star-formation history of the Universe out to high redshifts (Madau et al. 1996; Steidel et al. 1999). With the possible exception of observations made at sub-millimetre (submm) wavelengths, where a strong negative k-correction results in a redshift distribution dominated by high-z sources (e.g. Ivison et al. 2002; Smail et al. 2002; Chapman et al. 2005), this use of broad-band colour criteria to preselect high-z galaxy candidates is the most effective tool available for surveying the galaxy population at high redshift (Steidel et al. 2003).

Importantly too, whereas submm sources are unusual ultra-luminous objects (Chapman et al. 2005) with relatively low densities, LBGs represent a much larger population of comparatively 'normal' galaxies. For example, their luminosities, star-formation rates and level of obscuration are found to be in line with those of local star-forming galaxies (e.g. Steidel et al. 1996, 1999; Lowenthal et al. 1997; Pettini et al. 2001; Magdis et al. 2010). Additionally, compared to the selection of LAEs , which offer an alternative selection of galaxies at $z > 2$ via ground-based observations, the LBG selection allows the identification of galaxies across a broad and contiguous range of redshifts.

Steidel et al. (2003) presented a large survey of LBGs in the redshift range $2.5 < z < 3.5$, identifying ≈ 800 such galaxies. da Ângela et al. (2005a) took the Steidel et al. (2003) sample and used the clustering properties of the LBG population to constrain the cosmological density parameter, Ω_m, and the bulk motion properties of the large scale structure at $z \approx 3$. They measured a clustering amplitude for the LBGs of $r_0 = 4.48^{+0.17}_{-0.18}$ and based on the 2D clustering of the galaxies place constraints on the infall parameter of $\beta(z = 3) = 0.25^{+0.05}_{-0.06}$ and on the mass density of $\Omega_m(z = 0) = 0.55^{+0.45}_{-0.16}$. These results assume a velocity dispersion, which is degenerate with the infall parameter, of 400kms^{-1} and are based on small-scales with the transverse separation limited to $\sigma \lesssim 10\ h^{-1}$Mpc and so were somewhat limited. Bielby et al. (2011, Paper I) added to this presenting the first data from the VLT LBG Redshift Survey (VLRS). Adding ≈ 1,000 galaxies to the $z \approx 3$ sample of Steidel et al. (2003) data, they measured the clustering and dynamics of the $z \approx 3$ LBG population.

In this paper, we add to the previous results of the VLT LBG Redshift Survey (VLRS) presented in Paper I, Crighton et al. (2011, Paper II) and Shanks et al. (2011). Here we measure the clustering of the $z \approx 3$ LBG population. Throughout this paper, we use a cosmology given by $H_0 = 70$kms^{-1}, $\Omega_m = 0.3$, $\Omega_\Lambda = 0.7$ and $\sigma_8 = 0.8$. In addition distances are quoted in comoving coordinates in units of h^{-1}Mpc unless otherwise stated.

2 OBSERVATIONS

2.1 Survey overview

The VLRS presently encompasses nine separate fields centred on bright $z \approx 3$ QSOs. The imaging and spectroscopy for the first five fields were presented in Paper I. The observations described herein form the second part of the VLT LBG Survey. In order to facilitate an investigation of how $z \approx 3$ galaxies interact with gas in the intergalactic medium (IGM), the survey comprises observations of several target fields centred on bright $z > 3$ quasars, since features in the QSO spectra can provide information on the local IGM.

Paper I presented the first 5 fields of the survey, centred on the following quasars: Q0042–2627 ($z = 3.29$), J0124+0044 ($z = 3.84$), HE0940–1050 ($z = 3.05$), J1201+0116 ($z = 3.23$) and PKS2126–158 ($z = 3.28$), hereafter referred to by only the right-ascension component of these names. A spectroscopic survey of each of these quasar fields was carried out with the Visible Multi-Object Spectrograph (VIMOS) on the European Southern Observatory's Very Large Telescope (VLT) in Chile (during the ESO periods 75-79). Each field consisted of four sub-fields (individual pointings with the VLT spectrograph), except for HE0940 where only three sub-fields were available at the time of their publication. A VIMOS pointing has a field of view of $16' \times 18'$ (see §2.4.1), therefore each quasar field covered $\approx 32' \times 36'$, or ≈ 0.32 deg^2, except for HE0940 which with 3 sub-fields covered ≈ 0.24 deg^2.

0133), the NOAO Blanco 4m Telescope at Cerro Tololo Inter-American Observatory, Chile (programme IDs: 03B-0162, 04B-0022) and the ESO VLT, Chile (programme IDs: 075.A-0683, 077.A-0612, 079.A-0442).

† E-mail: rmbielby@gmail.com (RMB)

Table 1. A summary of the fields making up our $z \approx 3$ LBG survey. The table gives the name, coordinates and redshift of the QSO on which the fields are roughly centred, as well as the number of subfields (individual VLT VIMOS pointings) with spectroscopic data. The first block of fields were presented by Paper I, the second block are presented in this paper.

Field	RA[a]	Dec[a]	z [b]	Subfields	Reference
Q0042–2627	00:44:33.9	–26:11:21	3.29	4	Paper I
J0124+0044	01:24:03.8	+00:44:33	3.84	4	Paper I
HE0940–1050	09:42:53.4	–11:04:25	3.05	3	Paper I
J1201+0116	12:01:44.4	+01:16:12	3.23	4	Paper I
PKS2126–158	21:29:12.2	–15:38:41	3.28	4	Paper I
				19	
Q2359+0653	00:01:40.6	+07:09:54	3.23	4	This work
Q0302–0035	03:03:41.0	–00:23:22	3.23	4	This work
Q2231+0015	22:34:09.0	+00:00:02	3.02	3	This work
HE0940–1050	09:42:53.4	–11:04:25	3.05	6	This work
Q2348-011	23:50:57.9	-00:52:10	3.02	9	This work
				26	

[a] J2000 coordinates of QSO; not necessarily the exact centre of the observed field.
[b] redshift of the central quasar

Building on this initial dataset, we present the continuation of these observations since incorporating ESO periods 81 and 82. We have added a further 6 sub-fields to HE0940, tripling its previous area, as well as observations of 4 new fields, around the quasars Q2359+0653 ($z = 3.23$), Q0302–0035 ($z = 3.23$), Q2231+0015 ($z = 3.02$) and Q2348-011 ($z = 3.02$), with 4, 4, 3 and 9 sub-fields respectively. Table 1 summarises all the fields of the survey. This includes those presented by Paper I, covering 1.52 deg^2, and those presented here, which take the total observed area to 3.6 deg^2, more than doubling the previous size.

2.2 Imaging

2.2.1 Observations and data reduction

The selection of $z \approx 3$ LBG candidates was performed using photometry from optical broadband imaging. The imaging data for Q2359 and Q0302 were acquired with the Mosaic wide-field imager on the 4m Mayall telescope at Kitt Peak National Observatory (KPNO) in September 2005. The Q2231 data are from the Wide Field Camera on the 2.5m Isaac Newton Telescope (INT) on La Palma, and were observed in August 2005. All of these observations were carried out in the U, B and R bands.

The HE0940 and Q2348 data were acquired with the MegaCam imager on the 3.6m Canada-France-Hawai'i Telescope (CFHT). HE0940 was observed in the u, g, r, i and z bands in April 2004 as part of the observing run 2004AF02 (PI: P. Petitjean), whilst Q2348 was observed in the u, g, r and z bands over the period August-December 2004 as part of the observing run 2004BF03 (PI: P. Petitjean). Table 2 gives full details of all the imaging data. The instruments, filters and data reduction processes are described below.

The Mosaic imager at KPNO consists of 8 2k×4k CCDs arranged into an 8k×8k square. With a plate scale of 0.26″/pixel, this gives a field of view of 36′×36′. There are 0.5–0.7mm gaps between the chips, corresponding to gaps of 9–13″ on-sky, so a dithering pattern was used during the observations to provide complete field coverage. U, Harris B and Harris R filters were used, centred at 3552Å, 4298Å and 6380Å respectively.

The Mosaic image data were reduced using the `mscred` package in IRAF. The reduction process is described by Paper I, however we briefly outline the procedure here. Initially a master bias frame is produced for each night's observing. The dome flats and sky flats were then processed using the `ccdproc` and `mcspupil` routines, subtracting the bias and eliminating the faint 2600-pixel pupil image artefact. The object frames were processed similarly, subtracting the bias and pupil image, and then were flat-fielded using the dome and sky flats. Bad pixels and cosmic rays were masked out of the science frames using the `crreject`, `crplusbpmask` and `fixpix` procedures. Finally, the SWARP software package (Bertin et al. 2002) was used to resample and co-add the frames, producing a final science image.

The Wide Field Camera (WFCam) on the INT comprises 4 2k×4k CCDs. These are arranged into a 6k×6k block with a 2k×2k square missing. With $\approx 1'$ gaps between chips and a pixel scale of 0.33″/pixel, WFCam has a total FoV of $\approx 34' \times 34'$ (0.32 deg^2); however, accounting for the incomplete coverage of the field, the total observing area is reduced to 0.28 deg^2.

The WFCam observations of Q2231 were made using the RGO U, Harris B and Harris R filters. The RGO U filter has a central wavelength of 3581Å and a FWHM of 638Å, making it very similar to the U band filter used at KPNO (centre 3552Å, FWHM 631Å). The B and R band filters were the same as at KPNO. Therefore, given that the filters are so similar, we will use the same UBR selection criteria when identifying LBG candidates in either the Mosaic or WFCam datasets.

Initial data reduction, including bias removal, flat-fielding and photometric calibration, was performed by the Cambridge Astronomical Survey Unit (CASU). Astrometry

Table 2. Details of imaging observations for the LBG target fields presented in this paper.

Field	RA (J2000)	Dec (J2000)	Instrument	Band	Exposure (ks)	Seeing	Completeness (50% Ext/PS)	Dates
Q2359	00:01:44.85	+07:11:56.0	Mosaic (KPNO)	U	19.2	1.46″	24.76/25.18	29–30 Sep 2005
				B	7.2	1.45″	25.28/25.73	
				R	6.0	1.15″	24.74/25.20	
Q0301	03:03:45.27	-00:21:34.2	Mosaic (KPNO)	U	19.2	1.34″	24.93/25.34	29–30 Sep 2005
				B	6.4	1.28″	25.51/26.04	
				R	4.8	1.19″	24.59/25.17	
Q2231	22:34:28.00	+00:00:02.0	WFCam (INT)	U	54.0	1.23″	25.08/25.52	30 Aug 2005
				B	13.2	1.01″	25.88/26.12	
				R	19.2	1.01″	24.75/25.24	
HE0940	09:42:53.06	-11:02:56.9	MegaCam (CFHT)	u	6.8	0.99″	25.39/25.93	14, 21–27 Apr 2004
				g	3.1	0.86″	25.54/26.05	
				r	3.7	0.85″	25.08/25.65	
Q2348	23:50:57.90	-00:52:09.9	MegaCam (CFHT)	u	9.9	0.78″	25.97/26.62	19–20 Aug,
				g	5.5	0.79″	25.71/26.29	7–10 Nov,
				r	4.4	0.75″	25.22/25.80	15 Dec 2004

calibration and exposure stacking was performed using the SCAMP and SWARP packages.

MegaCam is a considerably larger instrument than Mosaic or WFCam, with 36 2k×4.6k CCDs arranged into a 18k×18k grid. With a high resolution of 0.187″/pixel this gives a 1°×1° FoV. The observations of HE0940 and Q2348 were carried out using the u*, g' and r' filters (referred to in this paper as u, g and r for convenience), with respective central wavelengths of 3743Å, 4872Å and 6282Å. These filters are significantly different from the filters used in our other fields and alternative LBG selection criteria are required for the MegaCam datasets.

2.2.2 Photometry

Photometric zeropoints for the imaging fields were determined from standard star observations carried out as part of each of the imaging runs. The standard star fields were reduced in the same way as the science frames to ensure consistency. Source detection in the science images was performed with SExtractor (Bertin & Arnouts, 1996), using a 1.5σ detection threshold and a 5-pixel minimum size.

The U_{Vega}, B_{Vega} and R_{Vega} band galaxy number counts in the Q0301 (diamonds), Q2231 (triangles) and Q2359 (squares) LBG fields are shown in the top panels of Fig. 1. Stars were removed from these counts at magnitudes brighter than ≈ 22 using a limit on the measured half-light radius of the sources. At fainter magnitudes, no attempt to remove stars from the counts was made, as the smallest extended sources become unresolved at the PSF of our fields at such magnitudes. We also show completeness estimates for each image in each field. These are estimated by placing simulated sources at random positions in a given image and measuring the fraction that are successfully extracted with SExtractor (using the same extraction parameters as used to create the full catalogues). In each case we estimate the completeness using both simulated point-sources and extended sources, where the extended sources are modelled by a de Vaucouleurs $r^{1/4}$ profile with a half-light radius of $r_{1/2} = 0.3''$. In both cases, the simulated source is convolved with the image PSF before being added to the observation.

The results of the completeness estimates for the UBR_{Vega} filter fields are shown in the lower panels of Fig. 1. The same symbols as the top panels are used for the different fields, whilst the dashed curves show the completeness estimates based on the extended sources and the solid curves show the completeness for the simulated point-sources. The 50% limits completion estimates are given in Table 2. Comparing the completeness measurements across the fields, the measurements are relatively consistent with the imaging in each field reaching comparable depths.

We show the galaxy number counts (top panels) and completeness estimates (lower panels) for the MegaCAM fields in Fig. 2. Again the symbols are consistent between top and lower panels with the diamonds showing the results for the HE0940 field and the triangles showing the Q2348 field. As before, the solid lines in the lower panels show the completeness estimates for the point-like sources and the dashed lines show the same for the extended sources (which use the same de Vaucouleurs profile as used for the UBR_{Vega} fields). Comparing the two fields to each other, the depths reached are comparable in each band, although the HE0940 is marginally less deep in the u band by ≈ 0.5 mag.

2.3 Candidate selection

2.3.1 UBR selection

In the Q2359, Q0302 and Q2231 fields, we selected LBG candidates based on their U, B and R photometry. The criteria used were the same as those used by Paper I, which are based on those of Steidel et al. (2003). There are 4 groups to the selection, designated LBG_PRI1, LBG_PRI2, LBG_PRI3 and LBG_DROP and defined as follows:

LBG_PRI1

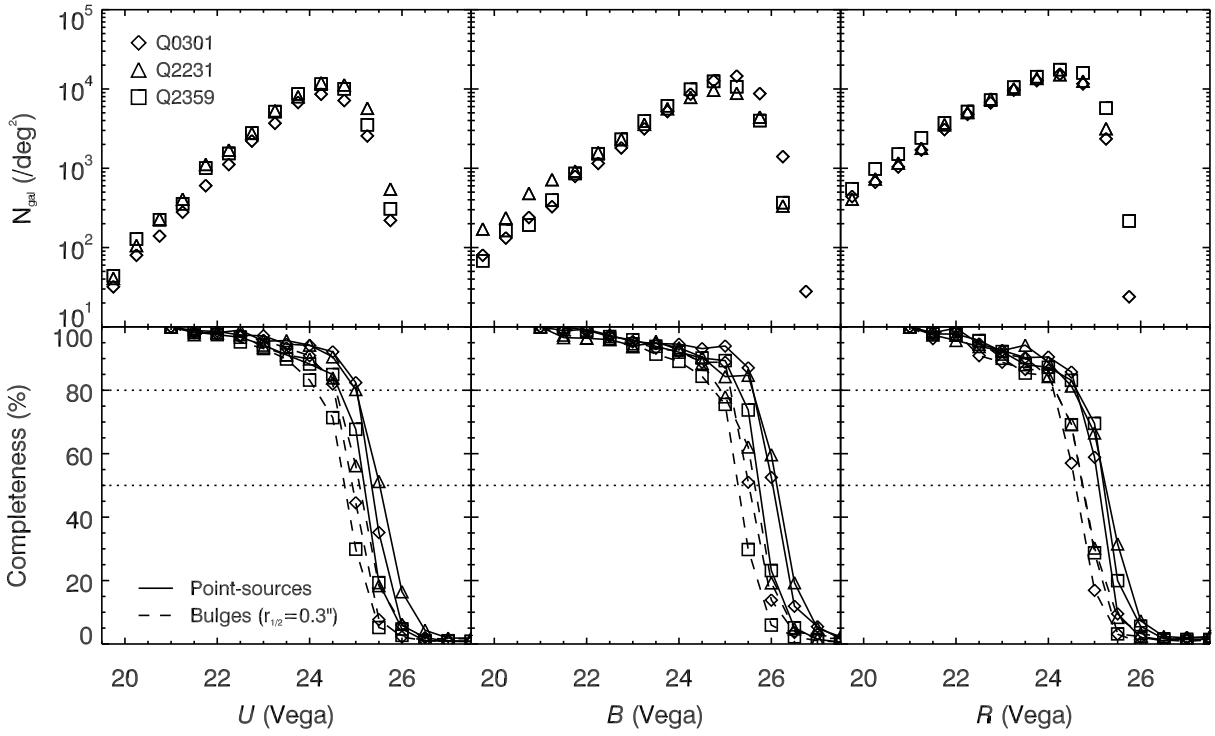

Figure 1. *Upper panel:* Galaxy number counts in the U (left), B (middle) and R (right) band imaging for the fields Q0301 (diamonds), Q2231 (triangles) and Q2359 (squares). *Lower panel:* Estimated completeness for each of the above bands based on simulated point sources (solid lines) and Vaucouleurs profile sources (dashed lines).

- $23 < R < 25.5$
- $0.5 < (U - B) < 4.0$
- $(B - R) < 0.8(U - B) + 0.6$
- $(B - R) < 2.2$

LBG_PRI2

- $23 < R < 25.5$
- $(U - B) > 0.0$
- $(B - R) < 0.8(U - B) + 0.8$
- $-1 < (B - R) < 2.7$
- $\notin$ LBG_PRI1

LBG_PRI3

- $23 < R < 25.5$
- $-0.5 < (U - B) < 0.0$
- $-1.0 < (B - R) < 0.8(U - B) + 0.6$
- $\notin$ {LBG_PRI1,LBG_PRI2}

LBG_DROP

- $23 < R < 25.5$
- $0.5 < (B - R) < 2.2$
- No detection in U

The first 3 groups represent an order of priority — that is, LBG_PRI1 candidates are considered more likely to be $z \approx 3$ LBGs than e.g. LBG_PRI3 candidates. This is because whereas LBG_PRI1 tends to select outliers in the UBR colour–colour plot, the lower priority groups select objects increasingly close to the colour region populated by stars and lower redshift galaxies, and therefore suffer from increased contamination from lower-redshift interlopers.

The fourth group is somewhat separate, being for galaxies which are not detected in the U band. Such sources may be excellent LBG candidates, since it may be that the presence of the Lyman limit in the U band has made the galaxy extremely faint in this band, such that it 'drops out' below the magnitude limit. However, the LBG_DROP population is also likely to suffer from contamination, in this case because objects with no counterpart in 1 of the 3 bands have a higher chance of being spurious sources.

Figs. 3, 4 and 5 show UBR colour–colour plots for Q2359, Q0302 and Q2231, respectively. In each plot, the LBG_PRI1, LBG_PRI2, LBG_PRI3 and LBG_DROP candidates are indicated. A model colour–redshift track is also plotted, showing the expected evolutionary path of a star-forming galaxy from $z = 0$ to $z = 4$. This was produced using the Bruzual & Charlot (2003) model, assuming a Chabrier IMF and an exponential SFR with e-folding time $\tau = 9$ Gyr. The model indicates that our selection criteria (across all the priority groups) is predicted to isolate galaxies in the range $\approx 2.5 < z < 3.8$. It also suggests that, of the sources that are confirmed as high-redshift LBGs, the LBG_PRI3s should typically be at a lower redshift than the LBG_PRI2s, which in turn should be at lower redshift than the LBG_PRI1s. Paper I noted that this trend was detected in their LBG sample.

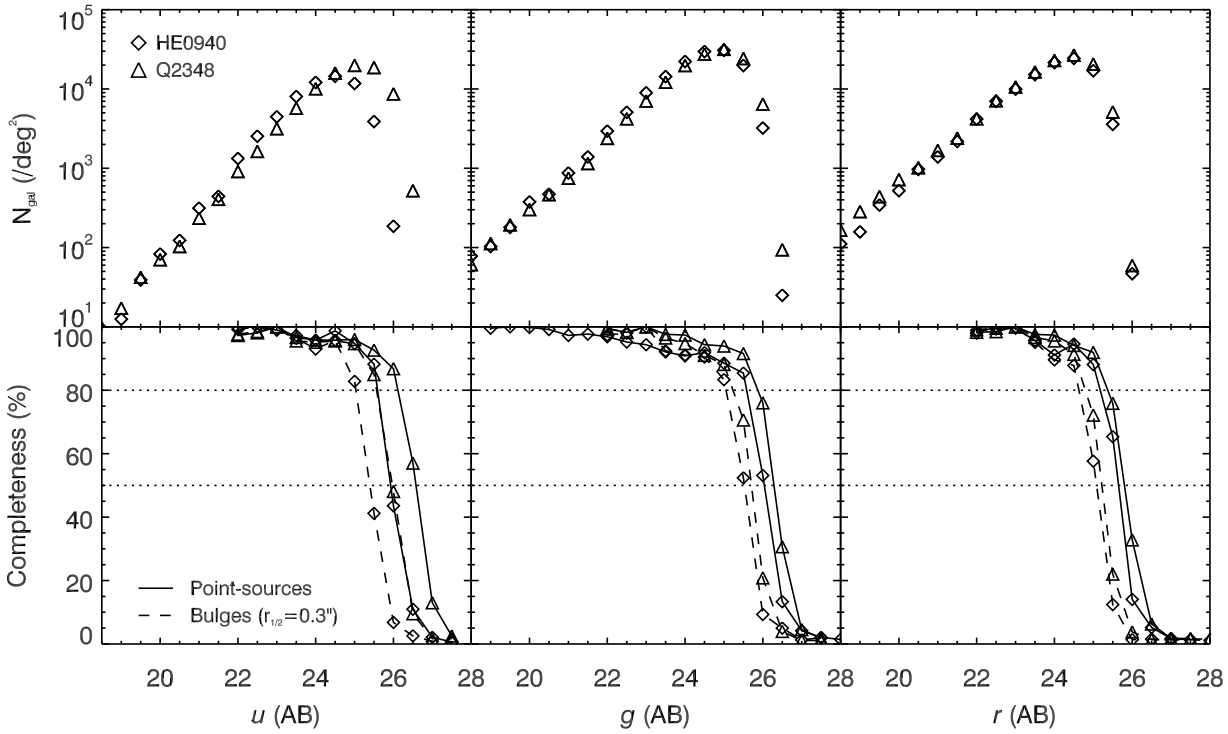

Figure 2. Number counts (top) and completeness estimates (bottom) in the u (left), g (middle) and r (right) bands from the MegaCAM imaging on the HE0940-1050 and Q2348-011 fields.

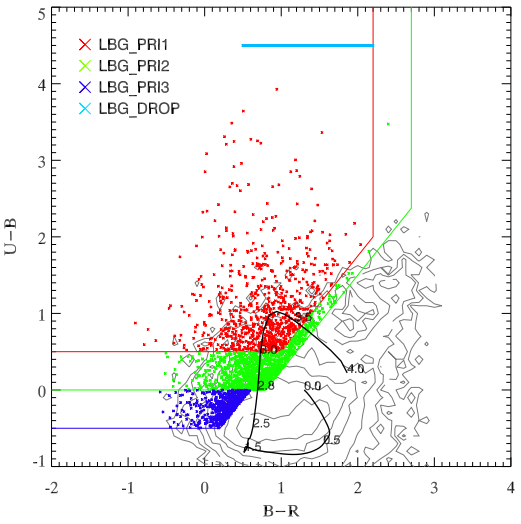

Figure 3. *UBR* colour-colour plot showing candidate selection in Q2359. Objects selected as LBG_PRI1, LBG_PRI2, LBG_PRI3 and LBG_DROP candidates are shown in different colours as indicated by the legend. The LBG_DROP candidates have been placed at $U - B = 4.5$. The contours show the colour distribution of the rest of the objects in the field.

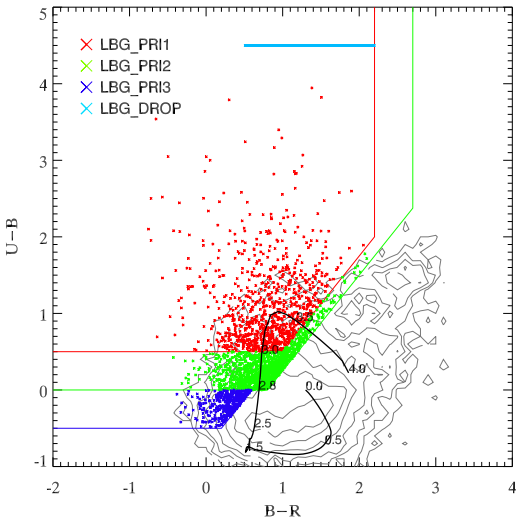

Figure 4. As for Fig. 3, but for Q0302.

2.3.2 ugr selection

In HE0940 and Q2348, LBG candidates were selected based on *ugr* photometry. We have therefore adapted the criteria outlined above to account for the different colour

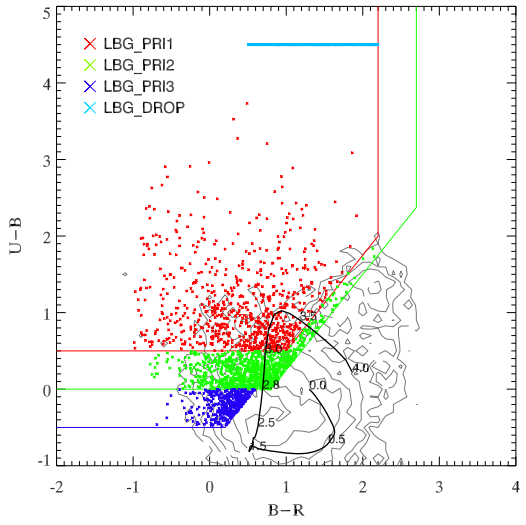

Figure 5. As for Fig. 3, but for Q2231.

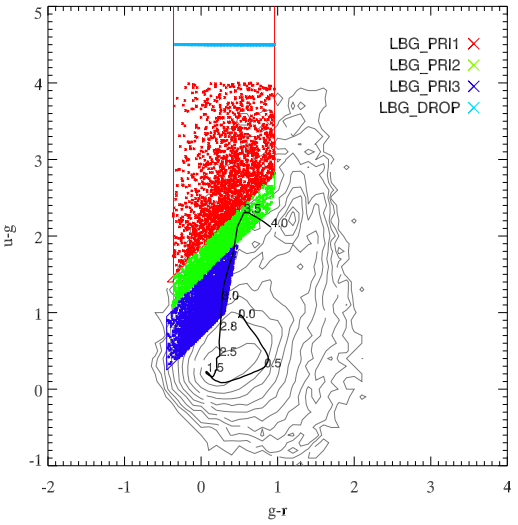

Figure 7. As for Fig. 6, but for Q2348.

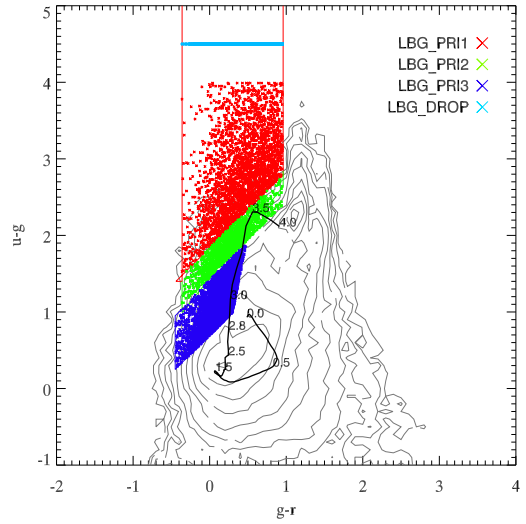

Figure 6. A *ugr* colour-colour plot showing the selection of candidates in HE0940. Symbols are as in Fig. 3.

bands. Again candidates were selected as either LBG_PRI1, LBG_PRI2, LBG_PRI3 or LBG_DROP, defined as follows:

LBG_PRI1

- $23 < r < 25$
- $1.4 < (u - g) < 4.0$
- $-0.36 < (g - r) < 0.96$
- $(g - r) < (u - g) - 1.88$

LBG_PRI2

- $23 < r < 25$
- $(u - g) > 1.0$
- $-0.36 < (g - r) < 0.96$
- $(g - r) < (u - g) - 1.44$
- $\notin$ LBG_PRI1

LBG_PRI3

- $23 < r < 25$
- $(g - r) < (u - g) - 0.7$
- $-0.45 < (g - r) < 0.2(u - g) + 0.1$
- $\notin$ {LBG_PRI1,LBG_PRI2}

LBG_DROP

- $23 < r < 25$
- $-0.36 < (g - r) < 0.96$
- No detection in u

Figs. 6 and 7 show the resulting candidates on *ugr* colour-colour plots, and Table 3 gives the numbers and sky densities of candidates in all 5 LBG fields.

2.4 Spectroscopy

2.4.1 Observations

The LBG candidates were targeted in spectroscopic follow-up observations with the VLT VIMOS spectrograph between September 2008 and December 2009, with programme IDs 081.A-0418(B) (Q2231), 081.A-0418(D) (Q2359), 081.A-0418(F) (Q0302), 082.A-0494(B) (HE0940) and 082.A-0494(D) (Q2348). The observations were done during dark time in generally good conditions with a typical seeing of $\approx 1''$ and an airmass of 1.0–1.3. Table 4 gives details of all the fields observed.

The VIMOS instrument (Le Fèvre et al. 2003) comprises four separate CCDs, each with a field of view of $7' \times 8'$. These four arms are arranged in a 2×2 grid with a $\approx 2''$ gap between each CCD, giving a total $16' \times 18'$ FoV as quoted previously. Of this 288 arcmin^2 field, 224 arcmin^2 is covered by the detector.

Our observations utilised the low resolution blue

Table 3. Numbers and sky densities of $z \approx 3$ LBG candidates in each of the fields. For each priority class, the first column shows the total number of candidates selected and the second, italicised column shows the density in arcmin^{-2}. The last two columns show the figures for all $z \approx 3$ LBG candidates.

Field	LBG_PRI1		LBG_PRI2		LBG_PRI3		LBG_DROP		All	
Q2359	795	*0.61*	1,130	*0.87*	549	*0.42*	2,235	*1.72*	4,709	*3.63*
Q0302	891	*0.69*	1,227	*0.95*	433	*0.33*	1,014	*0.78*	3,565	*2.75*
Q2231	748	*0.65*	948	*0.82*	424	*0.37*	514	*0.45*	2,634	*2.29*
HE0940	2,808	*0.78*	1,494	*0.42*	4,347	*1.21*	6,146	*1.71*	14,795	*4.11*
Q2348	1,843	*0.51*	1,624	*0.45*	4,808	*1.34*	1,850	*0.51*	14,795	*2.81*

(LR_Blue) grism and the order sorting blue (OS_Blue) filter, resulting in a wavelength range of 3700Å–6700Å, blazing at ≈4000Å. This wavelength range is ideal for our survey, detecting the Lyα line at $2.0 < z < 4.5$. The resolving power of the spectrograph in this configuration is $R = 180$ assuming a $1''$ slit (as used in these observations), which gives a resolution element of $\Delta\lambda \approx 22$Å at the blaze wavelength. The spectral dispersion is 5.3Å/pixel.

The slit masks were designed using the VMMPS software which is standard for VIMOS observations. The aims for mask design are (a) to maximise the number of observed targets, (b) to favour higher-priority targets and (c) to ensure slits are of sufficient size to allow a robust sky subtraction. Since these aims are frequently in conflict with one another, the mask design process is one of attempting to optimise the observations to satisfy all three as well as possible. Point (c) is addressed by setting a minimum slit length of $8''$ (40 pixels given the pixel scale of $0.205''$/pixel). Slit length was increased as much as possible where such an increase would not prevent the observation of an additional target — that is, where it did not conflict with point (a).

With the LR_Blue grism, each spectrum spans 640 pixels along the dispersion axis. Assuming a 40 pixel slit width as specified above, this would allow for a possible total of over 300 slits on the full 4k×2k detector. This is however not practically achievable given the density of LBG candidates, and is hampered further by the need to select high-priority candidates (point b), which have an even lower sky density. Our final slit masks therefore typically contain some 50–70 slits per quadrant.

2.4.2 Data reduction

The spectroscopic data have all been reduced using the VIMOS ESOREX reduction pipeline. Using bias frames, flat fields and arc lamp exposures taken for each mask during each observing run, the pipeline generates bias-subtracted, flat-fielded, wavelength-calibrated science frames consisting of a series of 2D spectra. Following Paper I we use the `imcombine` procedure in IRAF to combine the reduced frames from each observing block, generating a master science frame for each quadrant of each field. When combining the frames we use the `crreject` mode, designed to remove cosmic rays by rejecting pixels with significant positive spikes. We have also used the `avsigclip` rejection mode with a rejection threshold of 3σ, and find that our results are not significantly affected, suggesting that our results do not depend strongly on the parameters used to combine the science frames at this stage.

We extract 1D spectra from the reduced, combined 2D spectra using the IDL routine `specplot`. One-dimensional object and sky spectra are found by averaging across the respective apertures, and the sky spectrum is then subtracted from the object spectrum to give a final spectrum for the object.

In some cases there remain significant sources of contamination in the final object spectrum. These can arise from bad pixels, either in the object or sky aperture, from contamination from the zeroth order from other slits, or more frequently from the bright sky emission lines [O I] 5577Å, [Na I] 5990Å and [O I] 6300Å; in either case, the resulting contamination may manifest itself as either a positive or a negative spike in the spectrum. Such artefacts are, however, easily spotted during a routine inspection of the 2D spectrum.

2.5 Identification of targets

Every source targeted for spectroscopic observation is inspected visually, in both the 2D and 1D spectra, to determine where possible a redshift and classification. Sources are classified as either $z \approx 3$ Lyman-break galaxies, low-redshift galaxies, QSOs or Galactic stars. The LBGs are divided into those showing Lyα emission (designated LBe) and those showing Lyα absorption (LBa). QSOs are determined by the presence of broad emission features, in particular Lyα and CIV. Stars are classified by comparison to template spectra: in particular we check for A, F, G, K and M stars.

In determining the redshift and classification the spectral feature primarily used in the case of LBGs is the Lyα emission/absorption line at 1216Å; for lower redshift galaxies it is the [O II] emission line at 3727Å. In addition to these, some of the following features are used:
For $z \approx 3$ LBGs:

- Lyman limit, 912Å;
- Lyβ emission/absorption, 1026Å
- O VI 1032Å, 1038Å;
- Lyα forest, <1215.67Å;
- Lyα emission/absorption, 1215.67Å;
- Inter-stellar medium (ISM) absorption lines:
  - Si II 1260.4Å;
  - O I+Si II 1303Å;
  - C II 1334Å;

Table 4. Details of spectroscopic observations for the LBG target fields presented in this paper.

Field	Subfield	RA[a]	Dec[a]	Exposure[b]	Airmass	Seeing	Dates
Q2359	f1	00:01:09.94	+07:03:26.8	10	1.1 – 1.2	0.6 – 1.7″	23–25 Sep 2008
Q2359	f2	00:01:12.92	+07:16:39.2	10	1.1 – 1.3	0.6 – 1.3″	3, 20–21 Oct 2008
Q2359	f3	00:02:11.50	+07:15:33.9	10	1.2 – 1.4	0.6 – 1.3″	3, 21–25 Nov 2008
Q2359	f4	00:02:12.89	+07:02:19.1	10	1.2 – 1.3	0.5 – 1.1″	26–30 Nov 2008
Q2231	f1	22:34:28.19	–00:06:03.3	10	1.1 – 1.2	0.5 – 1.0″	23, 28 Oct 2008
Q2231	f2	22:34:28.55	+00:06:13.2	10	1.1 – 1.2	0.4 – 0.9″	21–22 Oct 2008
Q2231	f3	22:33:39.51	–00:06:10.8	10	1.1 – 1.2	0.5 – 1.0″	3 Aug; 27 Jul 2008
Q0302	f1	03:04:20.12	–00:14:28.8	12	1.1 – 1.3	0.7 – 1.2″	23, 31 Oct 2008
Q0302	f2	03:03:10.27	–00:16:18.7	12	1.1 – 1.2	0.7 – 1.5″	21–23 Nov 2008
Q0302	f3	03:03:15.41	–00:30:40.0	12	1.1 – 1.2	0.7 – 1.5″	25–26 Nov 2008
Q0302	f4	03:04:15.56	–00:28:59.1	12	1.1 – 1.2	0.7 – 1.2″	24 Sep; 1, 7 Oct 2008
HE0940	f4	09:42:10.00	–10:54:30.3	11.2	1.0 – 1.3	0.8 – 1.5″	1 Feb 2009
HE0940	f5	09:43:07.47	–11:24:50.3	11.2	1.0 – 1.3	0.7 – 1.4″	3 Feb 2009
HE0940	f6	09:41:59.99	–11:24:50.4	11.2	1.0 – 1.2	0.5 – 1.2″	20–21 Feb 2009
HE0940	f7	09:44:14.99	–11:24:49.9	11.2	1.0 – 1.2	0.5 – 1.3″	22, 24 Feb 2009
HE0940	f8	09:43:21.49	–10:41:00.5	11.2	1.0 – 1.2	0.5 – 1.0″	26–27 Feb 2009
HE0940	f9	09:42:09.99	–10:40:59.8	11.2	1.0 – 1.3	0.5 – 1.2″	2 Feb 2009
Q2348	f1	23:51:50.08	–00:54:21.9	11.5	1.1 – 1.2	0.5 – 1.7″	23–25 Jul 2009
Q2348	f2	23:50:45.09	–00:54:22.2	11.5	1.0 – 1.1	0.5 – 1.0″	19–20 Jul 2009
Q2348	f3	23:49:40.07	–00:54:22.6	11.5	1.0 – 1.2	0.4 – 0.8″	27 Jul 2009
Q2348	f4	23:51:50.12	–00:37:31.6	11.5	1.1 – 1.2	0.5 – 1.5″	20–21 Aug 2009
Q2348	f5	23:50:45.05	–00:37:31.5	11.5	1.0 – 1.2	0.7 – 1.4″	16–20 Sep 2009
Q2348	f6	23:49:40.00	–00:37:32.0	11.5	1.1 – 1.2	0.8 – 1.3″	24–25 Sep 2009
Q2348	f7	23:51:50.12	–01:07:31.4	11.5	1.1 – 1.2	0.7 – 1.0″	12, 20 Oct 2009
Q2348	f8	23:50:45.00	–01:07:32.0	11.5	1.1 – 1.3	0.7 – 1.3″	22 Nov, 10 Dec 2009
Q2348	f9	23:49:40.00	–01:07:32.0	11.5	1.1 – 1.3	0.8 – 1.5″	15–22 Nov 2009

[a] J2000 coordinates of subfield centre
[b] in ks

– Si IV doublet 1393Å & 1403Å;
– Si II 1527Å;
– Fe II 1608Å;
– Al II 1670Å;

- C IV doublet absorption, 1548-1550Å.

For low-z galaxies:

- CN absorption 3833Å;
- K-band absorption 3934Å;
- HK break 4000Å;
- Hδ emission 4102Å;
- Hβ emission/absorption 4861Å;
- O III emission 4959Å;
- O III emission 5007Å;

The presence of the HK break causes these interlopers to appear fairly frequently in our spectroscopic samples, since these features mimic the Lyman break on which our selection is based. The ISM absorption features listed above for LBGs are therefore of considerable importance in identifying genuine $z \approx 3$ galaxies. For every target which is identified, we assign a quality parameter to the redshift determined, in the range $0 \leqslant Q \leqslant 1$. A quality of $Q \leqslant 0.4$ indicates that a possible redshift has been determined, but is not considered a robust measurement. Above this, for LBGs, the quality parameters indicate that the redshift is based on the following features:

- $Q = 0.5$ — a spectral break with some weak Lyα emission/absorption and low-SNR ISM absorption features, or strong Lyα emission but with no detected continuum
- $Q = 0.6$ — a spectral break with high-SNR Lyα emission/absorption plus low-SNR ISM absorption features
- $Q = 0.7$ — a spectral break with high-SNR Lyα emission/absorption plus unambiguous, high-SNR ISM absorption features
- $Q \geqslant 0.8$ — a spectral break with high-SNR Lyα emission/absorption plus high-SNR absorption and emission lines

2.6 LBG sample

2.6.1 Sky densities and redshift distributions

In total, the VLRS now consists of 2,148 LBGs in 10,080 arcmin^2 (a density of 0.21 arcmin^{-2}). We show the sky distribution of LBGs from both Paper I, (open grey circles) and this paper (filled black circles) for all nine VLRS fields in Fig. 8. Known QSOs in the fields are also plotted (cyan stars). The total numbers of $Q \geqslant 0.5$ sources identified in each of the 5 fields presented here are given in Table 10. We present examples of the first six LBGs in each of the fields in

Table 5. Example LBG identifications in the Q2359+0653.

ID	R.A. (J2000)	Dec.	$U-B$	$B-R$	R	$z_{Ly\alpha}$	z_{ISM}	Q_{ID}
VLRS J000139.85+070221.66	0.4160563	7.0393505	0.63	0.76	23.5500	2.4762	2.4682	0.5
VLRS J000133.54+070127.57	0.3897395	7.0243263	0.13	0.15	25.3600	2.5707	2.5603	0.5
VLRS J000118.84+070106.55	0.3285175	7.0184855	1.29	1.21	23.8900	3.0374	3.0294	0.5
VLRS J000131.05+070106.56	0.3793770	7.0184898	0.58	0.65	25.3900	2.7910	2.7967	0.5
VLRS J000141.27+070106.35	0.4219468	7.0184293	1.51	0.12	24.3800	2.6508	2.6428	1.0
VLRS J000140.69+070044.11	0.4195270	7.0122533	0.47	0.65	23.7800	2.8162	2.8082	0.5
...	...	...	...	...	...	...	...	...
...	...	...	...	...	...	...	...	...

Table 6. Example LBG identifications in the Q0301-0035.

ID	R.A. (J2000)	Dec.	$U-B$	$B-R$	R	$z_{Ly\alpha}$	z_{ISM}	Q_{ID}
VLRS J030434.85-001549.27	46.1452103	-0.2636854	0.59	0.61	24.4700	2.6132	2.6041	0.7
VLRS J030435.40-001607.15	46.1474953	-0.2686527	1.56	1.45	23.4100	2.5969	2.6157	0.7
VLRS J030439.49-001619.35	46.1645317	-0.2720422	1.08	0.62	24.5100	2.9570	2.9490	0.5
VLRS J030438.22-001647.63	46.1592560	-0.2798966	-0.22	0.37	23.8600	2.7098	2.7292	0.6
VLRS J030435.86-001654.14	46.1494179	-0.2817046	0.80	0.92	25.0700	2.8887	2.8807	1.0
VLRS J030426.38-001701.38	46.1099281	-0.2837157	0.21	0.56	24.4900	2.4651	2.4571	0.6
...	...	...	...	...	...	...	...	...
...	...	...	...	...	...	...	...	...

Table 10. Numbers of objects in each target field spectroscopically identified (at $Q \geqslant 0.5$) as either high-z LBGs, $z < 2$ galaxies, QSOs or stars.

Field	$z \approx 3$ LBGs	$z < 2$ galaxies	QSOs	Stars
Q2359	180 (0.20 arcmin^{-2})	127	3	8
Q0302	204 (0.23 arcmin^{-2})	131	10	13
Q2231	114 (0.17 arcmin^{-2})	128	6	18
HE0940	373 (0.28 arcmin^{-2})	260	3	48
Q2348	335 (0.17 arcmin^{-2})	183	8	48
Total	1,206 (0.21 arcmin^{-2})	829	30	135

Table 11. Redshift distribution statistics for spectroscopically confirmed, $Q \geqslant 0.5$ LBGs in the 5 observed fields. In each case the mean redshift $\bar{z}$ (with standard error), median redshift $\tilde{z}$ and standard deviation σ of the distribution is given.

Field	$\bar{z}$	$\tilde{z}$	σ
Q2359	2.77 ± 0.02	2.72	0.33
Q0302	2.64 ± 0.02	2.61	0.28
Q2231	2.65 ± 0.03	2.62	0.29
HE0940	2.81 ± 0.02	2.77	0.33
Q2348	2.87 ± 0.02	2.87	0.36
Total	2.78 ± 0.01	2.74	0.34

Tables 5 to 9. The full tables will be made available online at http://star-www.dur.ac.uk/∼bielby/vlrs/.

For the $z > 2$ sample, the VLRS now consists of 1,016 $Q = 0.5$, 545 $Q = 0.6$, 334 $Q = 0.7$, 153 $Q = 0.8$ and 100 $Q = 0.9$ galaxies.

Fig. 9 shows the $n(z)$ distributions of all sources with measured redshifts in each of the 5 LBG fields. The figure shows that LBGs in HE0940 and Q2348, where LBGs were selected in *ugr*, have higher average redshifts than in the *UBR*-selected fields, suggesting that the *ugr* criteria bias the selection toward higher z. It is also notable from Table 10 that the *ugr* selection appears to include more Galactic stars. Future *ugr*-selected LBG surveys may wish to alter our colour criteria to better avoid stellar interlopers.

Fig. 9 also shows $n(z)$ for the subsets of sources with $Q \geqslant 0.6$ and $Q \geqslant 0.7$. We note that in any given field, the *distributions* of sources at $Q \geqslant 0.5$, $Q \geqslant 0.6$ or $Q \geqslant 0.7$ are approximately the same — the LBGs with higher ID qualities are not skewed to lower or higher redshift, for example — suggesting that the redshift distributions shown are fairly robust. The average redshifts and standard deviations are given in Tab. 11. The redshift distribution of the full LBG sample has a mean redshift of 2.78 ± 0.01 and a standard deviation of 0.34, and is shown in Fig. 10.

Fig. 11 shows, as anticipated in §2.3, that candidates selected as LBG_PRI1 lie at higher redshift than the LBG_PRI2 candidates, which are in turn at higher redshift than LBG_PRI3s. Quantitatively, we find that the LBG_PRI1s have a mean redshift of $\bar{z} = 2.83 \pm 0.02$, the LBG_PRI2s have $\bar{z} = 2.71 \pm 0.02$ and the LBG_PRI3s have $\bar{z} = 2.61 \pm 0.02$. The LBG_DROP candidates are shown in a separate panel for clarity, and have the highest mean redshift of all the groups, with $\bar{z} = 2.93 \pm 0.02$.

Table 7. Example LBG identifications in the HE0940-1050.

ID	R.A. (J2000)	Dec.	$u-g$	$g-r$	r	$z_{Ly\alpha}$	z_{ISM}	Q_{ID}
VLRS J094225.83-105744.50	145.6076355	-10.9623623	2.57	0.35	23.6400	2.8804	2.8810	0.5
VLRS J094240.69-105753.44	145.6695251	-10.9648447	1.88	0.35	24.1100	3.1456	3.1376	0.5
VLRS J094220.01-105900.05	145.5833588	-10.9833469	—	-0.14	24.3800	2.2010	2.1930	0.5
VLRS J094217.39-105923.95	145.5724640	-10.9899855	—	0.16	23.8500	2.5153	2.5073	0.5
VLRS J094217.51-105935.92	145.5729675	-10.9933100	—	0.79	24.2600	2.8139	2.8119	0.6
VLRS J094242.29-110121.16	145.6762085	-11.0225439	0.74	-0.03	23.9900	2.4613	2.4595	0.5
...	...	...	...	...	...	...	...	...
...	...	...	...	...	...	...	...	...

Table 8. Example LBG identifications in the Q2231+0015.

ID	R.A. (J2000)	Dec.	$U-B$	$B-R$	R	$z_{Ly\alpha}$	z_{ISM}	Q_{ID}
VLRS J223439.00+000341.29	338.6625061	0.0614693	—	0.72	24.1500	2.8428	2.8291	0.6
VLRS J223459.87+000308.07	338.7494507	0.0522424	1.01	0.78	23.7400	2.4879	2.4789	0.5
VLRS J223450.20+000232.38	338.7091675	0.0423284	—	1.92	23.7800	2.8934	2.8927	0.7
VLRS J223459.03+000051.79	338.7459717	0.0143855	—	0.54	24.3200	2.8037	2.7957	0.9
VLRS J223442.76-000028.59	338.6781616	-0.0079414	0.32	1.01	23.6900	2.1897	2.1817	0.5
VLRS J223447.81-000041.63	338.6991882	-0.0115636	—	0.87	24.8000	2.8874	2.8735	0.5
...	...	...	...	...	...	...	...	...
...	...	...	...	...	...	...	...	...

2.7 Galaxy redshifts

In star-forming galaxies such as those presented here, the observed Lyα emission is redshifted relative to the intrinsic galaxy redshift, while the interstellar absorption lines are blue-shifted (see e.g. Shapley et al. 2003). In order to improve the accuracy of the galaxy redshifts, we must account for these offsets. We do this using one of following 3 expressions, following the method of Adelberger et al. (2005a).

$$z' = \bar{z} + 0.070\Delta z - 0.0010(\bar{z} - 2.7) \quad (1)$$

$$z' = z_{\rm em} - 0.0033 - 0.0050(z_{\rm em} - 2.7) \quad (2)$$

$$z' = z_{\rm abs} - 0.0022 - 0.0015(z_{\rm abs} - 2.7) \quad (3)$$

where z' is the intrinsic galaxy redshift, $z_{\rm em}$ is the redshift of the Lyα emission line, $z_{\rm abs}$ is the redshift of the ISM absorption lines, $\bar{z} = (z_{\rm em} + z_{\rm abs})/2$ and $\Delta z = z_{\rm em} - z_{\rm abs}$. We note that we do not use the more recent relations of Steidel et al. (2010); Rakic et al. (2011) as these are based on lower redshift BX-selected galaxies.

Eqn. 1 relies upon having a reasonably robust measurement of both the Lyα emission and the ISM features; we therefore use it only for those LBGs with high-quality redshift IDs ($Q \geqslant 0.6$), as ISM features are only weakly detected in the lower-quality LBGs. For the low-Q sources we instead use Eqn. 2, which determines an intrinsic redshift based on the Lyα emission line alone.

For the LBGs showing no Lyα emission the intrinsic redshift is calculated based on the ISM absorption features and using Eqn. 3, with $z_{\rm abs} = z_{\rm Ly\alpha} = z_{\rm ISM}$.

Paper I estimated the errors on the LBG redshifts using simulated spectra. Here, we extend the investigation into the redshift errors in our survey by using duplicate redshift measurements. The fields presented here, particularly Q2348, were designed with overlapping regions and consequently there are some LBG candidates which were observed in more than one mask. In cases where these duplicated targets are confirmed as LBGs, this provides two independent redshift measurements for the same LBG, and thus a direct observational test of the redshift measurement accuracy.

Fig. 12 shows the Δz distribution for the LBGs with duplicate observations, where $\Delta z = |z_1 - z_2|$ is the difference between the two redshift measurements. 20 objects were classified as LBGs in two separate observations; of these, Fig. 12 indicates that 16 had fairly small errors of $\Delta z < 0.02$ (of which 13 had very small errors of $\Delta z < 0.005$), while 4 had considerably larger errors. In addition to these 20 objects, we have also searched a region of our Q0302 field which overlaps with Steidel et al. (2003) survey for any LBGs which were identified in both surveys: we find 3 such objects, and the redshift differences for these galaxies are also indicated in Fig. 12.

The standard deviation of the 20 Δz values measured for duplicate observations in our survey is $\sigma = 0.036$, corresponding to a velocity error of $\approx$2,800 km s^{-1} assuming a redshift of $z = 2.8$, the sample mean. However, this misrepresents the true error in our redshift measurements, since it is skewed by the 4 sources with very high Δz. These 4 values do not represent redshift *measurement* errors, rather catastrophic outliers. In the cases where we find large Δz values, the error does not arise due to uncertainty in the peak wavelength, but in uncertainty over which spectral feature

Table 9. Example LBG identifications in the Q2348-011.

ID	R.A. (J2000)	Dec.	$u-g$	$g-r$	r	$z_{Ly\alpha}$	z_{ISM}	Q_{ID}
VLRS J235206.92-005646.70	358.0288391	-0.9463067	1.30	0.30	24.4600	3.1430	2.3707	0.5
VLRS J235200.98-005903.11	358.0040894	-0.9841969	2.50	0.46	24.2400	3.3532	3.3435	0.5
VLRS J235201.68-010002.18	358.0069885	-1.0006067	1.23	0.31	24.9700	2.8632	2.8603	0.5
VLRS J235155.14-010104.04	357.9797363	-1.0177902	1.66	0.15	23.8600	2.7523	2.7503	0.7
VLRS J235209.28-005535.49	358.0386658	-0.9265237	1.28	0.13	24.0700	2.6274	2.6194	0.7
VLRS J235202.62-004747.89	358.0109253	-0.7966368	2.11	0.32	24.2700	3.0640	3.0646	0.5
...	...	...	...	...	...	...	...	...
...	...	...	...	...	...	...	...	...

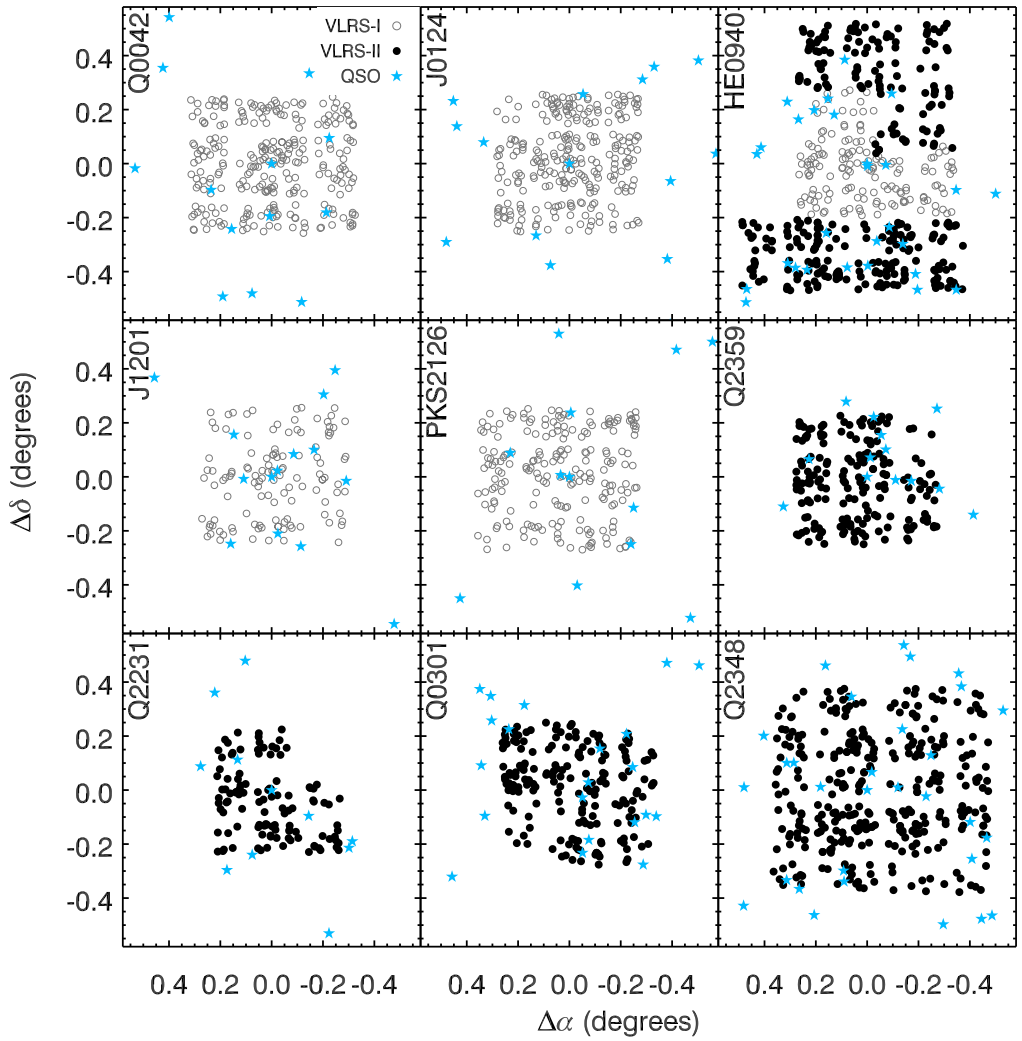

Figure 8. Sky distribution of LBGs and QSOs in the VLRS fields. Grey open circles show LBGs presented in Paper I, black filled circles show LBGs identified in the current work and cyan stars show known QSOs.

is actually Lyα. In these cases, different spectral features have been identified as Lyα, leading to large Δz. These are therefore better characterised as *identification* errors, in that two different solutions have been reached in the two observations.

For the 16 duplicated targets shown in Fig. 12*b*, the same feature has been identified as Lyα and therefore the Δz for these objects gives an indication of the measurement error. The standard deviation for these objects is $\sigma = 0.005$, corresponding to $\Delta v \approx 380$ km s^{-1}.

The suggestion, therefore, is that $\approx$80% of our LBGs have redshift measurement errors of $\Delta v \leqslant 400$ km s^{-1}, while the other 20% may have larger errors. This problem, however, disproportionately affects sources with an ID quality

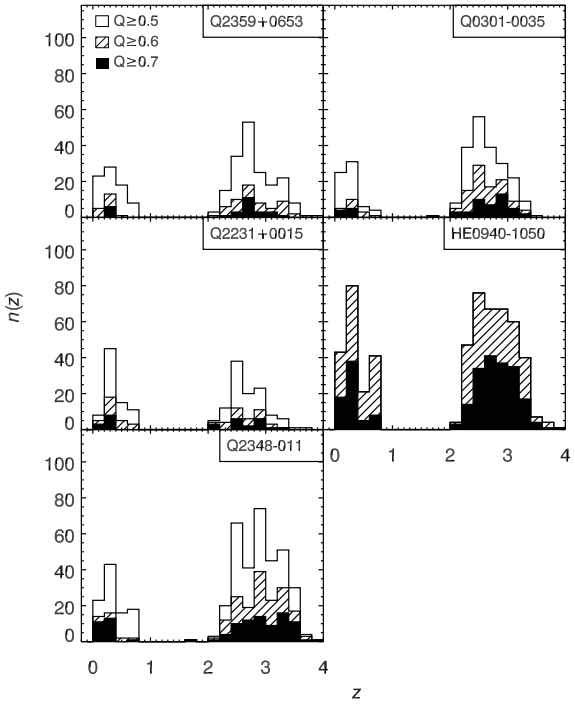

Figure 9. Redshift distributions of identified sources in each of the target fields. In each panel we show the distribution for the full sample ($Q \geqslant 0.5$), as well as for the $Q \geqslant 0.6$ (hashed) and $Q \geqslant 0.7$ (filled) subsets, where Q is the redshift quality parameter.

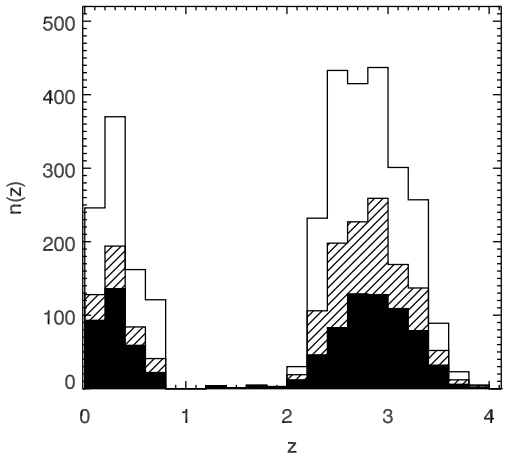

Figure 10. Redshift distribution of all identified sources in our 5 target fields. The distribution is shown for the full sample (i.e., sources with $Q \geqslant 0.5$; unfilled), as well as for the $Q \geqslant 0.6$ (hashed) and $Q \geqslant 0.7$ (filled) subsets, where Q is the redshift quality parameter.

parameter $Q = 0.5$: of the four sources with large Δz, one was given a quality factor of 0.5 for both redshift measurements, while the other 3 have one measurement with $Q = 0.5$ and another with $Q = 0.6$; in the latter cases the $Q = 0.6$ measurement is fairly robust while the $Q = 0.5$ measurement is less reliable. Therefore, the LBGs which may suffer from large errors can be excluded by removing the $Q = 0.5$ LBGs from the sample.

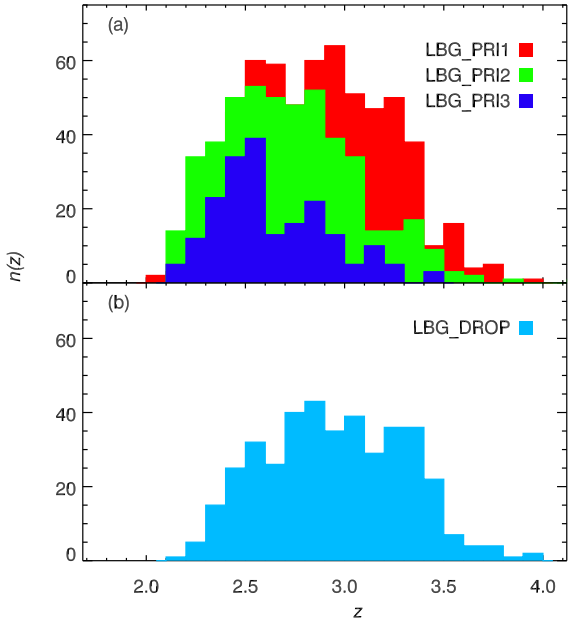

Figure 11. Redshift distribution of all identified sources our 5 target fields, separated by initial candidate priority. Panel *(a)* shows the LBG_PRI1, LBG_PRI2 and LBG_PRI3 classes, while the LBG_DROPs are shown separately in panel *(b)* for clarity. Colours are as in Figs. 3–6.

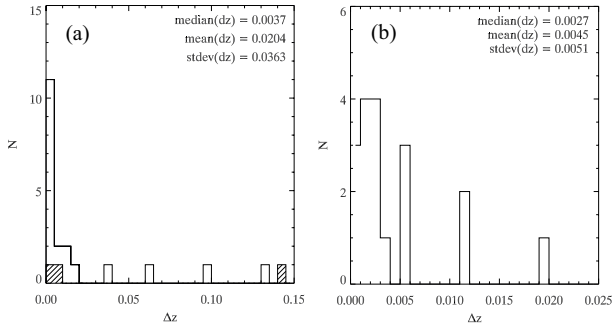

Figure 12. The distribution of redshift measurement errors, Δz, calculated using the LBGs which were observed twice in our survey and therefore have two independent redshift measurements. In panel *(a)* we show the full distribution, in panel *(b)* a close-up of the distribution at $z < 0.025$. Overplotted as a hashed histogram in panel *(a)* are the Δz values for 3 sources in our survey which had a redshift in the survey of Steidel et al. (2003).

2.7.1 Composite spectra

We have calculated composite spectra using the $z > 2$ VIMOS low-resolution galaxy data. The composite spectra were generated by averaging over the spectra after having corrected the spectra for the instrument response and having masked skylines. In addition, each individual spectrum is normalised by its median flux in the rest-frame wavelength range $1250\mathring{A} \leqslant \lambda \leqslant 1450$ before being combined to form the composite.

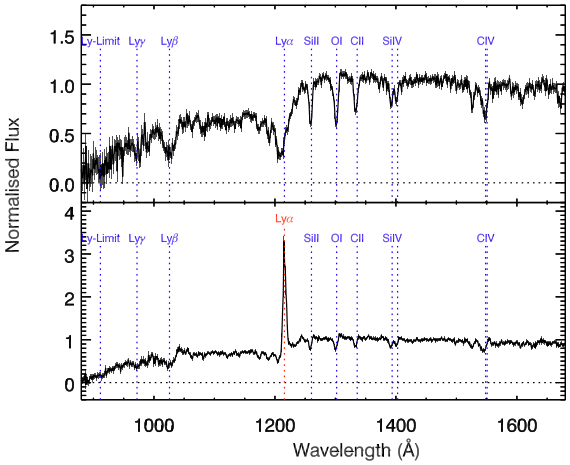

Figure 13. Composite spectra for galaxies showing Lyα in absorption (top) and emission (bottom), with ISM absorption lines clearly detected.

In Fig. 13 we show stacked spectra for the LBGs, separated into those showing Lyα in emission (lower panel) and in absorption (upper panel). These stacked spectra show the average ultraviolet SED of a $z \approx 3$ LBG with excellent signal-to-noise, and the quality of these spectra provide an indication of the robustness of our LBG identifications. In Fig. 14, we show 3 separate composite spectra for sources classed as LBe's with quality IDs of $Q = 0.5$, $Q = 0.6$ and $Q \geqslant 0.7$. These spectra reflect the quality criteria set out in §2.5 well, with increasing quality spectra clearly showing increasingly high signal-to-noise in both Lyα emission and ISM absorption features. The absorption features are only weakly detected in $Q = 0.5$ LBGs.

2.7.2 Quasars & AGN

We have identified 30 $z > 2$ AGN and QSOs in our spectroscopic sample by the presence of broad emission lines. Their spectra are shown in Fig. 15. All of the QSOs show broad Lyα emission and most (at least 3/4) also show broad C IV λ1549, a high-ionisation emission line often used to constrain the dynamics and size of the broad-line region in QSOs as well as the virial mass of the black hole (Fine et al. 2010, and references therein). Many of the QSOs also show broad O VI λ1035 and N V λ1241, the latter usually being blended with Lyα. These emission lines are indicated in each panel of Fig. 15.

Several other emission lines are detected in some of the QSO spectra but are not marked in the figure. Lyβ λ1026 is clearly seen in panel (d), where it may be asymmetrically broadened to longer wavelengths by the presence of relatively weak O VI λ1035. Panel (n) shows an emission line peaking at 1029Å, likely suggesting a blend between Lyβ and O VI.

Panels (i) and (p) both show very broad emission at $\approx$ 1500Å. These emission features cover the expected wavelength range of an Fe III multiplet, however they considerably brighter than would be expected for these Fe III lines (Vestergaard & Wilkes, 2001; Sigut, Pradhan & Nahar, 2004), therefore the origin of these emission lines is unclear.

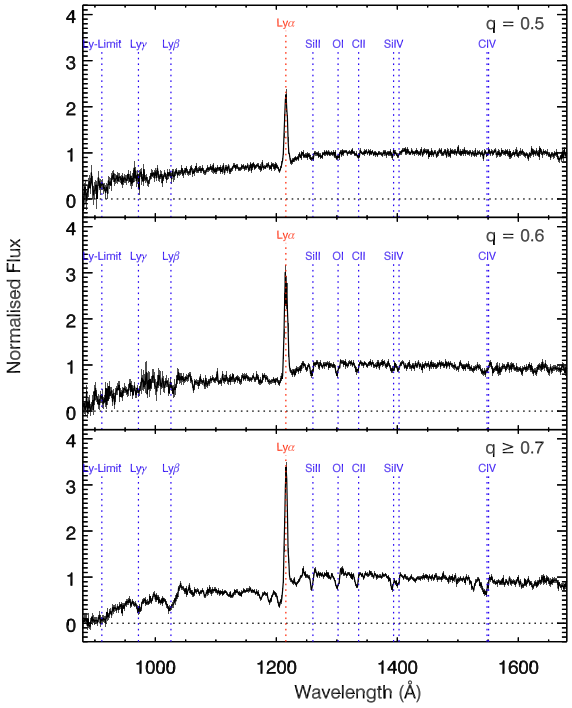

Figure 14. Composite spectra for galaxies classified as LBe's, separated by ID quality parameter Q. Those with $Q = 0.5$ (upper panel) show comparatively weak Lyα emission and marginal detections of ISM absorption lines. Moving to higher quality values, the strength of the Lyα line increases and we also see high-SNR absorption features. Note that the spectra are not flux calibrated.

O I λ1304 emission appears in panels (g), (t) and (s) (but is difficult to see in the figure), however in all 3 cases the peak of the emission appears at slightly longer wavelength than the nominal 1304Å. This may indicate a blend with Si II λ1308, but is more likely due to the low-ionisation lines (which include O I) arising from a separate part of the broad line region to the high-ionisation lines and thus having a marginally higher redshift (Constantin et al. 2002). Finally, panels (a), (c), (l), (m), (o), (r), (s) and (t) all show clear emission at $\approx$ 1400Å, arising from a blend of the Si IV λ1396 and O VI] λ1402 transitions.

3 CLUSTERING OF $z \approx 3$ LBGS

We now analyse the clustering of the $z \approx 3$ LBGs. As well as offering insights into the growth and evolution of structure in the Universe, we aim to measure the dynamics of the $z \approx 3$ galaxy population, i.e. peculiar velocities and gravitational infall, to inform the analysis of the gas-galaxy relationship via LBG-Ly-α forest cross-correlation (see Paper II).

We note that for some of the observed fields, there is some variation in the magnitude cuts applied in selecting the candidates for spectroscopic observation. The analysis of the clustering is therefore limited to those galaxies with $R < 25$. Aside from this magnitude cut, all galaxies with $Q \geqslant 0.5$ are included throughout this analysis.

In the analysis that follows, we measure the galaxy clus-

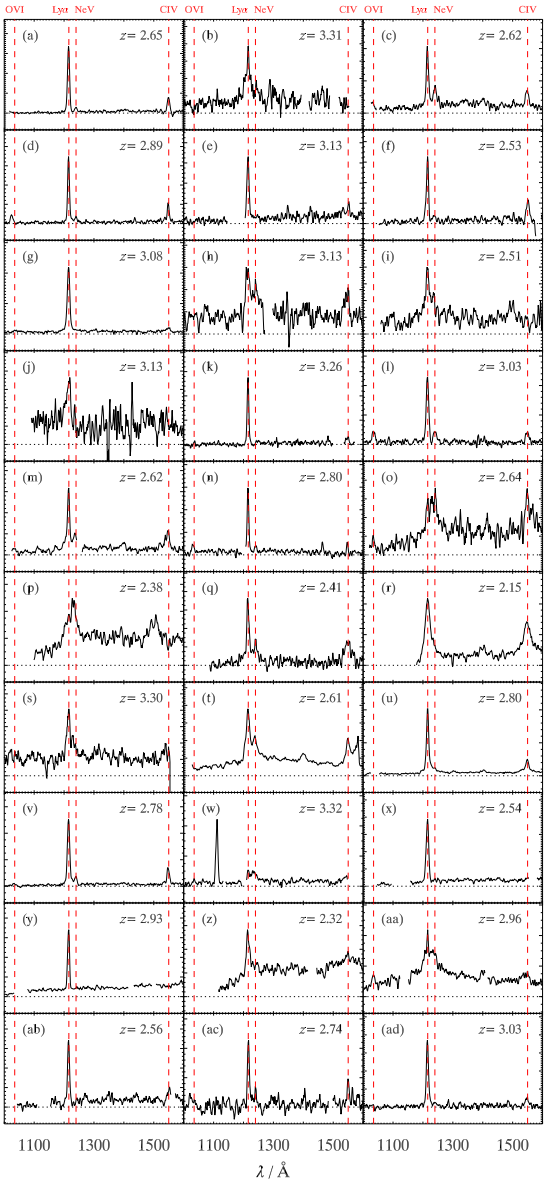

Figure 15. Rest-frame VIMOS spectra for the QSOs detected in the 5 fields presented. The y-axis scales differ from panel to panel, but the dotted line marks zero flux in each case. Dashed red lines indicate the wavelength of O VI, Lyα, Ne V and C IV emission. Gaps in the spectra indicate that an artefact has been masked out.

tering as a function of galaxy-galaxy separation using the Landy-Szalay estimator:

$$\xi(x) = \frac{\langle \mathrm{DD}(x)\rangle - 2\langle \mathrm{DR}(x)\rangle + \langle \mathrm{RR}(x)\rangle}{\langle \mathrm{RR}(x)\rangle} \qquad (4)$$

where $\xi(x)$ is the clustering as a function of separation x, $\mathrm{DD}(x)$ is the number of galaxy-galaxy pairs at that separation, $\mathrm{DR}(x)$ is the number of galaxy-random pairs and $\mathrm{RR}(x)$ is the number of random-random pairs. This is estimated using a random catalogue that consists of 20× as many random points as data points and that covers an identical area. The redshift distribution of the random catalogue is set using a polynomial fit to the data.

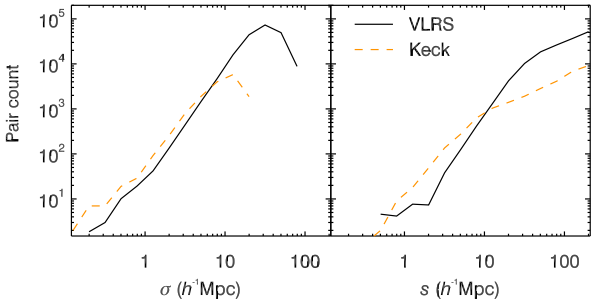

Figure 16. Pair counts (DDs) as a function of pair separation in the transverse, σ, and 3D Hubble, s, directions. The Keck data (dashed orange curves) provide better sampling at small scales, whilst the VLRS data (solid black curves) provides sampling at larger scales that is not provided by previous data.

We focus on fitting the auto-correlation function in the semi-projected, $w_p(\sigma)$, and full 2-D, $\xi(\sigma,\pi)$, forms, where σ and π are the separation of two galaxies transverse and parallel to the line-of-sight. But we shall also study the LBG z-space correlation function, $\xi(s)$, where the signal can be significantly higher at large scales.

For $\xi(\sigma,\pi)$ in particular, we also consider the combined sample of the VLRS data with the Keck LBG data of Steidel et al. (2003). The Keck data consists of 813 $z \approx 3$ galaxies and offers higher sampling rates than the VLRS, but across smaller field sizes ($\approx 8'$). This is illustrated in Fig. 16 where the solid black line shows the VLRS pair counts (DD) as a function of separation in the transverse direction, σ (left hand panel), and the 3-D separation, $s = \sqrt{\sigma^2+\pi^2}$ (right hand panel). In both panels the Keck pair counts are shown by the dashed orange line. Fig 16 shows that the VLRS pair counts in both the transverse and 3-D distance are significantly higher than in the previous Keck sample at $\sigma, s \gtrsim 10\mathrm{h}^{-1}\mathrm{Mpc}$.

3.1 Semi-projected correlation function, $w_p(\sigma)$

We first estimate the LBG clustering using the semi-projected correlation function, $w_p(\sigma)$. This gives the clustering at fixed transverse separation, σ, integrated over line-of-sight distance, π, approximately independent of the effect of peculiar velocities and is given by:

$$w_p(\sigma) = 2\int_0^\infty \xi(\sigma,\pi)d\pi \qquad (5)$$

where $\xi(\sigma,\pi)$ is the 2-D auto-correlation function. We integrate $\xi(\sigma,\pi)$ over the range $0 < \pi < \pi_{\max}(\sigma)$, where $\pi_{\max}(\sigma)$ is given by the maximum of $1000(1+z)/H(z)$ and 15σ at a given sky separation σ (consistent with Adelberger et al. 2003; da Ângela et al. 2005a).

In the calculation of $w_p(\sigma)$, we make a correction for the effect of 'slit collisions', following Paper I. Any object observed with VIMOS takes up an area on the detector of at least 40×640 pixels (§2.4.1), corresponding to $8'' \times 130''$ on-sky. Other candidates lying within this area can therefore not be observed (unless the area is revisited), and as a

result, pairs of LBGs at small separations are systematically missed by our survey. This effect will reduce the measured LBG auto-correlation at small separations. Paper I quantified this effect by comparing the angular auto-correlation function of photometrically selected LBG candidates and spectroscopically observed candidates. Using their result, we correct for this effect in our LBG survey by weighting DD pairs at $\theta < 8'$ according to the weighting factor given by

$$W(\theta) = \frac{1}{1 - (0.0738 \times \theta^{-1.052})} \quad (6)$$

where θ is the angular separation in arcminutes.

In addition to the slit collision correction, a further correction - the integral constraint - is required to compensate for the effect of the limited field sizes. For this we follow the commonly used approach of using the random-random pair distributions, which have been constructed to match the survey geometry, to determine the magnitude of the integral constraint. This method has been well described by a number of authors (e.g. Groth & Peebles 1977; Peebles 1980; Roche et al. 1993; Baugh et al. 1996; Phleps et al. 2006), with Phleps et al. (2006) in particular providing a detailed discussion in relation to the projected correlation function, and we provide a brief description of the calculation here.

The measured correlation function is given by the true correlation function minus the integral constraint, $\mathcal{I}$:

$$w_m(\sigma) = w_t(\sigma) - \mathcal{I} \quad (7)$$

Assuming a power-law form for the the real-space clustering, the true projected clustering is fit by:

$$w_p(\sigma) = C r_0^{\gamma} \sigma^{1-\gamma} \quad (8)$$

where r_0 is the real-space clustering length and γ is the slope of the real-space clustering function, $\xi(r)$, which is characterised by a power-law of the form:

$$\xi(r) = \left(\frac{r_0}{r}\right)^{\gamma} \quad (9)$$

The factor C is given by:

$$C = \left(\frac{\Gamma\left(\frac{1}{2}\right) \Gamma\left(\frac{\gamma-1}{2}\right)}{\Gamma\left(\frac{\gamma}{2}\right)} \right) \quad (10)$$

where Γ is the Gamma function. Given this framework, the integral constraint can be estimated from the mean of the random-random pair counts, $\langle RR \rangle$, and the slope of the correlation function, such that:

$$\frac{\mathcal{I}}{C r_0^{\gamma}} = \frac{\Sigma \langle RR(\sigma) \rangle \sigma^{1-\gamma}}{\Sigma \langle RR(\sigma) \rangle} \quad (11)$$

Quantifying errors on the auto-correlation function has been performed using Poissonian, jack-knife and random realisation error estimates. The Poisson errors are given by:

$$\Delta\xi = \frac{(1+\xi)}{\sqrt{\langle DD \rangle / 2}} \quad (12)$$

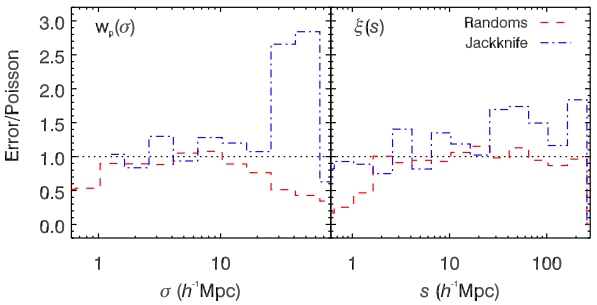

Figure 17. Ratio of the random mock (red dashed histogram) and the jack-knife (blue dot-dashed histogram) error estimates to the Poisson errors as a function of separation for the projected correlation function (left panel) and the redshift space autocorrelation function (right panel). The results are shown for the VLRS sample only.

The jack-knife errors were computed by splitting the data into individual fields, with the large fields (i.e. HE0940 and Q2348) being split into two fields each. We therefore have 11 different jack-knife realisations with a single field (or half-field) being excluded in each realisation.

The random realisation error estimates incorporate 100 random catalogues with the same number of objects as the real data. We then calculate the correlation function using these random realisations to calculate the $\langle DD \rangle$ pairs and take the standard deviation of the results as the uncertainty on the measurement.

In Fig. 17, we compare the above error estimates for $w_p(\sigma)$ and the redshift space clustering function, $\xi(s)$ (see section 3.2), showing the ratio of the jack-knife and random realisation methods to the Poisson result. The estimates are consistent with each other over scales from $\approx 1-25\ h^{-1}$Mpc. In what follows, we therefore use the Poisson estimates at separations of $< 25\ h^{-1}$Mpc and jack-knife estimates at separations $> 25\ h^{-1}$Mpc.

The projected auto-correlation function for the VLRS sample (black circles), the Keck sample (orange squares; Steidel et al. 2003) and the two combined (cyan triangles) is shown in Fig 18. The plotted data include the integral constraint correction, which we estimated as $\mathcal{I}_{wp} = 5.29$ and $\mathcal{I}_{wp} = 7.18$ for the VLRS and Keck data respectively.

Based on this we estimate a clustering length of the entire VLRS sample of $r_0 = 3.32 \pm 0.41\ h^{-1}$Mpc (comoving) with a slope of $\gamma = 1.53 \pm 0.13$. The Keck result on it's own gives a result of $r_0 = 3.98 \pm 0.32\ h^{-1}$Mpc with $\gamma = 1.58 \pm 0.13$, whilst the combined VLRS+Keck data gives $r_0 = 3.75 \pm 0.24\ h^{-1}$Mpc with a slope of $\gamma = 1.55 \pm 0.09$. These r_0 results are comparable to the clustering of star-forming galaxies at lower redshifts (e.g. Blake et al. 2009; Bielby et al. 2010).

Comparing to other measurements of the $z \approx 3$ LBG clustering length, Giavalisco & Dickinson (2001) measured $r_0 = 5.0 \pm 0.7\ h^{-1}$Mpc for $R_{AB} < 25$ LBGs, but for a relatively small number of galaxies (≈ 400). Building on that sample, Adelberger et al. (2003) measured $r_0 = 3.96 \pm 0.29\ h^{-1}$Mpc with a slope of $\gamma = 1.55 \pm 0.15$ at $R_{AB} < 25.5$. We note that with the same sample, but a different method, Adelberger et al. (2005b) found a higher clustering strength of $r_0 = 4.5 \pm 0.6\ h^{-1}$Mpc. Subsequently, Cooke et al. (2006)

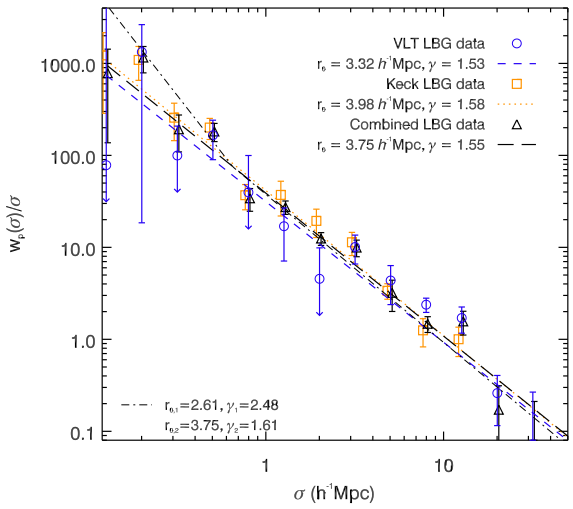

Figure 18. Projected auto-correlation function, $w_p(\sigma)/\sigma$, for the VLT LBG sample (black circles). The result for the $2.5 < z < 3.5$ Keck LBG sample is shown by the orange squares and error bars for both results are estimated using Poisson errors. The best fit power laws for both the VLT (solid black line) and Keck (dashed orange line) are shown, with clustering amplitudes of $r_0 = 3.32 \pm 0.41$ h^{-1}Mpc and $r_0 = 3.98 \pm 0.32$ h^{-1}Mpc, with slopes of $\gamma = 1.53 \pm 0.13$ and $\gamma = 1.58 \pm 0.13$ respectively. The cyan triangles show the combined result and the dotted cyan line the best fit to this of $r_0 = 3.75 \pm 0.24$ h^{-1}Mpc with a slope of $\gamma = 1.55 \pm 0.09$.

measured the clustering of $z \approx 3$ LBGs in fields around damped Lyα absorbers and found a lower clustering strength of $r_0 = 2.65 \pm 0.48$ h^{-1}Mpc with a slope of $\gamma = 1.55 \pm 0.40$ at $R_{AB} < 25$. Overall, our result therefore appears consistent with other measurements, although marginally lower than the Giavalisco & Dickinson (2001); Adelberger et al. (2003, 2005b) results, which are all based on the same - or a subset of the same - sample.

The above estimates are based on spectroscopically confirmed samples and a number of clustering measurements exist based on photometric samples. For example Foucaud et al. (2003) measured $r_0 = 5.9 \pm 0.5$ h^{-1}Mpc from the angular correlation function of $R_{AB} < 24.5$ LBGs from the Canada-France Deep Fields Survey (McCracken et al. 2001), a higher r_0 than the spectroscopic samples, but also a significantly brighter magnitude cut. Additionally, Adelberger et al. (2005b) measured $w(\theta)$ for photometrically selected LBGs and found $r_0 = 4.0 \pm 0.6$ h^{-1}Mpc for $R < 25.5$ LBGs, consistent with our results. Hildebrandt et al. (2007) measured $r_0 = 4.8 \pm 0.3$ h^{-1}Mpc for $22.5 < R_{\rm Vega} < 25.5$ galaxies in the GaBoDS data. Subsequently, Hildebrandt et al. (2009) measured $r_0 = 4.25 \pm 0.13$ h^{-1}Mpc for CFHTLS LBGs at $r_{AB} < 25$ and using photo-z from HYPERZ (Bolzonella et al. 2000). Again, our estimate for r_0 is marginally lower than these measurements, however as noted the photometric selections will be prone to a certain level of uncertainty caused by contamination corrections.

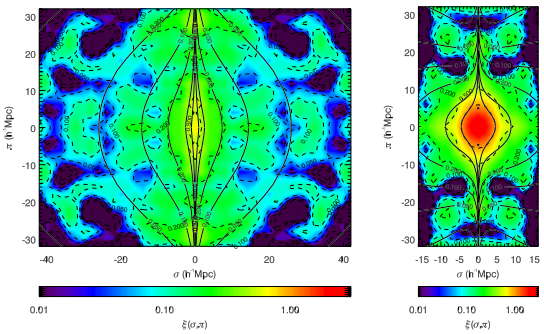

Figure 19. The two-dimensional auto-correlation function, $\xi(\sigma, \pi)$ results for the VLRS (left) and Keck (right) data samples individually. The shaded contour map and dashed contour lines show the measured $\xi(\sigma, \pi)$ in each case.

3.2 2D Auto-Correlation Function, $\xi(\sigma, \pi)$

As discussed above, integrating along the redshift/line-of-sight direction leaves the semi-projected correlation function, $w_p(\sigma)$, independent of the effects of galaxy peculiar motions. We now attempt to fit the full 2D correlation function, $\xi(\sigma, \pi)$, to retrieve the kinematics of the galaxy population and to make new estimates of r_0.

As before, we use the Landy-Szalay estimator to calculate the correlation function but now as a function of both transverse separation, σ, and line-of-sight separation, π. We use the same random catalogues matching the survey fields as used for the calculation of the projected correlation function. We again calculate the integral constraint for the data sets using the random catalogues via:

$$\frac{\mathcal{I}}{r_0^\gamma} = \frac{\Sigma \langle RR(s) \rangle s^\gamma}{\Sigma \langle RR(s) \rangle} \qquad (13)$$

where $s = \sqrt{(}\sigma^2 + \pi^2)$. This gives values of $\mathcal{I}_\xi = 0.036$ and $\mathcal{I}_\xi = 0.064$ for the VLRS and Keck data samples respectively.

Fig. 19 shows the result for the VLRS data (left-hand panel), which provides a greater handle on the large scale ($s \gtrsim 10h^{-1}$Mpc) clustering, the Keck data (right panel), which provides greater sampling on small scales. Fig. 20 shows the VLRS and Keck results combined. In each case, $\xi(\sigma, \pi)$ was calculated in linear 2 h^{-1}Mpc bins and subsequently smoothed with a fwhm of 2 h^{-1}Mpc.

For both the VLRS and Keck samples, we see the 'finger of god' effect at small σ scales in which the clustering power is extended in the π direction. This effect is a combination of galaxy peculiar velocities and measurement errors on the galaxy redshifts. In addition, in the VLRS a flattening of the clustering measurement at large scales is evident, which is caused by dynamical infall of galaxies.

We now fit models of the clustering to these results, initially assuming a single power-law for $\xi(r)$ and allowing r_0 and the kinematical parameters to vary. We take the r_0 and γ estimates from the $w_p(\sigma)$ fit as the starting point in fitting the 2D clustering. The kinematics are characterised by two parameters: the velocity dispersion in the line of sight direction $\sqrt{\langle w_z^2 \rangle}$ and the infall parameter, β. The model we use incorporating the galaxy kinematics is described in full by Hawkins et al. (2003) and Paper I. For the VLRS

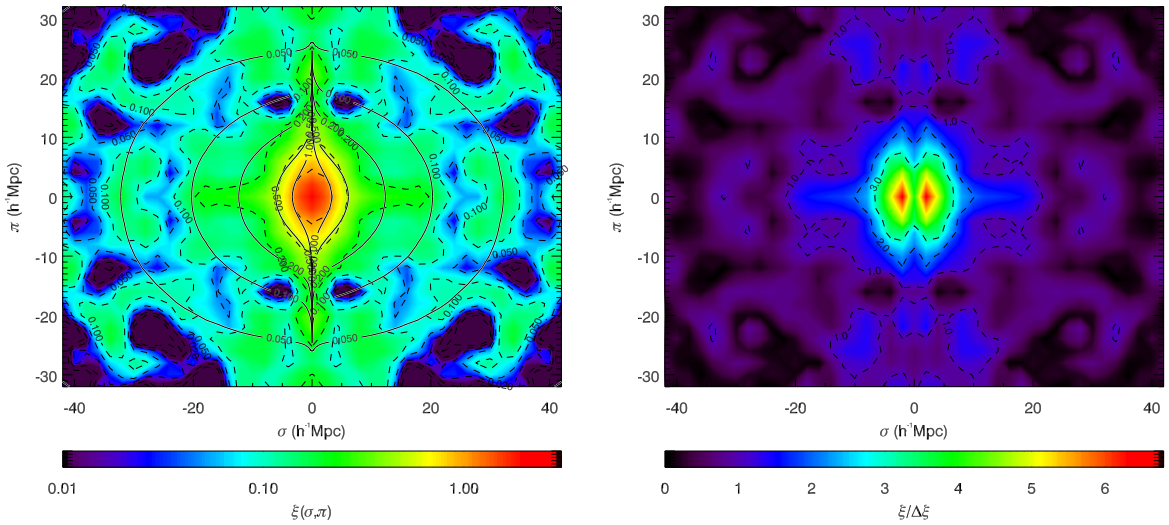

Figure 20. The two-dimensional auto-correlation function, $\xi(\sigma,\pi)$ results for the VLRS sample (left) and the signal-to-noise on the result (right). The shaded contour map and dashed contour lines show the measured $\xi(\sigma,\pi)$, whilst the solid contour lines give the best fitting model.

and the combined samples we fit over the range $1.0 \leqslant s \leqslant 25\ h^{-1}$Mpc, whilst for the Keck data by itself we limit the fit to the scales $1.0 \leqslant s \leqslant 15\ h^{-1}$Mpc (note that the largest single field available in the Keck data is $\approx 15\ h^{-1}$Mpc).

For the two samples individually, we find that it is difficult to place reasonable constraints on both the velocity dispersion and the infall together. With the VLRS data (over the range $1 \leqslant (\sigma,\pi) \leqslant 25\ h^{-1}$Mpc), we find $\beta(z=3) = 0.3^{+1.7}_{-0.3}$ and $\sqrt{\langle w_z^2\rangle} = 1700^{+2000}_{-900}$kms^{-1}, the low signal-to-noise on small scales limiting the fit accuracy. We experimented with adding a uniform error distribution out to $\pm$12000kms^{-1} to the Gaussian velocity dispersion (c.f. Fig. 12) but this made little difference in the σ,π range fitted. Fitting the Keck data gives best fit values of $\beta(z=3) = 0.85^{+0.30}_{-0.35}$ and $\sqrt{\langle w_z^2\rangle} = 700 \pm 220$kms^{-1}. We note that da Ângela et al. (2005a) performed a similar fit to the Keck data for $\beta(z=3)$, but kept a constant velocity dispersion of $\sqrt{\langle w_z^2\rangle} = 400$kms^{-1}, finding a value for the infall parameter of $\beta(z=3) = 0.15^{+0.20}_{-0.15}$. By also setting the velocity dispersion to a value of 400kms^{-1}, we find that we retrieve a comparable result to da Ângela et al. (2005a), highlighting the degeneracy between the velocity dispersion and the infall parameter.

Ultimately, fitting the VLRS $\xi(\sigma,\pi)$ is hindered by a lack of signal-to-noise on small scales, whilst the fit to the Keck data is hindered by the small size of the fields. We thus combine the two datasets and fit the full LBG sample in the same manner as with the individual samples. The fit is performed in the range $1 < s < 25\ h^{-1}$Mpc and we allow the velocity dispersion and the infall parameter to vary. The resulting fit gives a velocity dispersion of $\sqrt{\langle w_z^2\rangle} = 540^{+180}_{-200}$kms^{-1} and an infall parameter of $\beta(z=3) = 0.32 \pm 0.20$. We show the χ^2 contours for the fit in the $\beta(z=3) - \sqrt{\langle w_z^2\rangle}$ plane in Fig. 21 (the contours represent the 1σ, 2σ and 3σ confidence limits). From this figure, the degeneracy can be seen between $\sqrt{\langle w_z^2\rangle}$ and β, where increasing β similarly increases the best fit velocity dispersion. The best fitting results are plotted over the contour maps of the $\xi(\sigma,\pi)$ measurements in Fig. 20 (dashed contours). As with the data, we see the finger-of-god and large scale flattening effects in the fitted models.

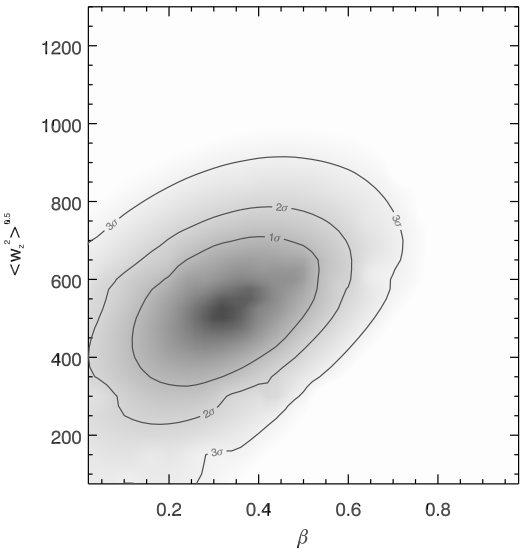

Figure 21. Fitting contours for peculiar velocity and bulk inflow based on the combined VLRS+Keck $\xi(\sigma,\pi)$. The best fitting result is given by $\beta(z=3) = 0.32 \pm 0.20$ and $\sqrt{\langle w_z^2\rangle} = 540^{+180}_{-200}$kms^{-1}.

3.3 Redshift-space correlation function, $\xi(s)$.

In order to check the consistency of our measurements, we now compare the model fit obtained from $w_p(\sigma)$ and $\xi(\sigma,\pi)$ to the measured redshift-space auto-correlation function $\xi(s)$. Again we use the Landy-Szalay estimator and quote errors based on Poisson estimates. The $\xi(s)$ results

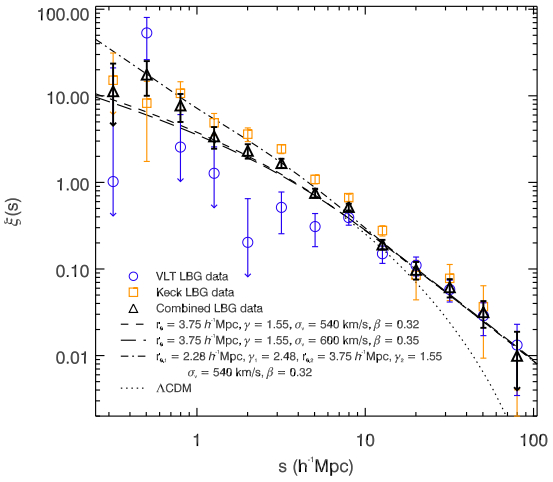

Figure 22. Redshift space correlation function, $\xi(s)$, for the VLRS (open blue circles), Keck (orange squares) and combined (black triangles) samples. The short and long dashed curves show single power law model fits to the combined sample based on fits to $w_p(\sigma)$ and $\xi(\sigma,\pi)$. The dash-dot curve gives a double power law model fit, whilst the dotted curve at large scales shows the predicted ΛCDM clustering.

for the VLRS, Keck and combined LBG samples are shown in Fig. 22. We also plot the single power law estimate of the intrinsic clustering from our fits to the VLT+Keck $\xi(\sigma,\pi)$ (dotted line) and the result of this power-law after applying the best fit values for β and $\sqrt{\langle w_z^2\rangle}$ (dashed line). The final fit incorporating the galaxy dynamics is marginally low compared to the data-points, but is easily consistent within the error bars.

Our measurements of β and $\sqrt{\langle w_z^2\rangle}$ are consistent with the previous measurements using the first VLT dataset (Paper I). As discussed in Paper I, the median measurement error on the galaxy lines on the VLT VIMOS spectra is $\approx$ 360kms^{-1}. In addition, an uncertainty of $\approx$ 200kms^{-1} is introduced by the transformation from outflow redshifts to intrinsic galaxy redshifts using Eqns 1, 2 and 3. The final contribution to the velocity dispersion is from the intrinsic peculiar velocities of the galaxies. Using the GIMIC simulations (Crain et al. 2009) we have analysed the mean velocity dispersion of LBG-like galaxies and find a value of $\approx$ 100kms^{-1}. Combining these three elements in quadrature, we would expect a pairwise velocity dispersion of $\sqrt{\langle w_z^2\rangle} \approx \sqrt{2} \times \sqrt{(360\mathrm{kms}^{-1})^2 + (200\mathrm{kms}^{-1})^2 + (100\mathrm{kms}^{-1})^2} \approx 600\mathrm{kms}^{-1}$. This is within the 1σ error contours for a slightly higher value of β in Fig. 21. This value is also reasonably consistent with the VLRS $\xi(s)$ estimate (see Fig. 22).

A ΛCDM $\xi(r)$ with standard values for the cosmological parameters (flat space, $\Omega_m = 0.27$, $H_0 = 70\mathrm{kms}^{-1}\mathrm{Mpc}^{-1}$ and $\Omega_b h^2 = 0.022$) is also compared to the combined data in Fig. 22 where the linear model has been normalised to the combined $\xi(s)$ at 10 h^{-1}Mpc. There are currently some claims that non-Gaussianity is detected at $z \approx 1$ in NRAO VLA Sky Survey radio source (Xia et al. 2010) and Luminous Red Galaxy (LRG) datasets (Thomas et al. 2011; Sawangwit et al. 2011; Nikoloudakis et al. In Prep). The evidence generally comes comes from detecting large scale excess power via flatter slopes for angular correlation functions. Since non-Gaussianity is easier to detect at high redshift this motivates checking the LBG $\xi(s)$ for an excess. We have already noted that the slope from w_p and $\xi(\sigma,\pi)$ at $\gamma = 1.55$ is much flatter than the canonical $\gamma = 1.8$. This slope is also flatter than the $z \approx 1$ LRG large-scale $w(\theta)$ slope of Nikoloudakis et al. (In Prep). We see that the VLRS does give reasonably accurate measurements for $25 < s < 100$ h^{-1}Mpc and that the observed LBG $\xi(s)$ shows a $\approx 2.5\sigma$ excess over the ΛCDM model in this range. Even when the marginally smaller integral constraint for the ΛCDM model is assumed the discrepancy remains at $\approx 2\sigma$. We conclude that there is some evidence for an excess over the standard ΛCDM model but independent LBG data is needed to confirm this on the basis of the redshift space correlation function. The statistical error on the LBG $w(\theta)$ from Paper I is smaller but the flat power-law here is only seen to $\theta = 10'$ or $r = 13-14$ h^{-1}Mpc and this is not enough to decide the issue.

3.4 Double power-law correlation function models

We next look to see if a more complicated model than a power-law for $\xi(r)$ is required. This is motivated firstly because Paper I noted that there was an increase in the slope at ≈ 1 h^{-1}Mpc in the LBG angular auto-correlation function, $w(\theta)$, suggestive of the split between the 1-halo and 2-halo terms in the halo model of clustering. Although this result is uncertain due to quite significant low redshift contamination corrections, such features have been seen in lower redshift galaxy samples, particularly for LRGs at $z \approx 0.5$ (e.g. Ross et al. 2007; Sawangwit et al. 2011). Given the improved power of the VLRS, it is interesting to see if there is any evidence of a change in the slope at small scales in $\xi(s)$ and $w_p(\sigma)$ in our $z \approx 3$ LBG sample.

We therefore show in Fig. 18 a double power-law model for w_p with the same power-law slopes as fitted by Paper I to the LBG $w(\theta)$. We have reduced the amplitude by $\approx$ 20% to match approximately the large-scale amplitude fitted to the VLRS and Keck combined data. This is within the systematic uncertainties of the $w(\theta)$ measurement. Although certainly not required by the w_p data this double power-law cannot be rejected by the combined w_p data, giving a reduced χ^2 of 1.77 (marginally smaller than the reduced χ^2 obtained for a single power law of 1.84).

In Fig. 22 we now compare to $\xi(s)$ the same double power-law $w(\theta)$ model with the $\approx$ 20% reduced amplitude. Again with a velocity dispersion of 540kms^{-1} and $\beta = 0.32$ we see that the model cannot be rejected by the data. We note that if we use a $\langle DD\rangle$ / $\langle DR\rangle$ estimator the VLRS $\xi(s)$ result shows increased power at large scales and the flatter slope of the double power-law model here provides a better fit.

We note that other authors have also reported a turn-up in the clustering at small scales in high redshift galaxy samples. For instance Ouchi et al. (2005) reports that $z = 4$ LBG $w(\theta)$ shows a steepening below ≈ 0.2 h^{-1}Mpc or $\approx 10''$ at $z = 4$. If both results are unaffected by contamination then it could argue for an evolutionary growth in this break scale between $z = 4$ and $z = 3$.

Certainly there is plenty to motivate expanding surveys

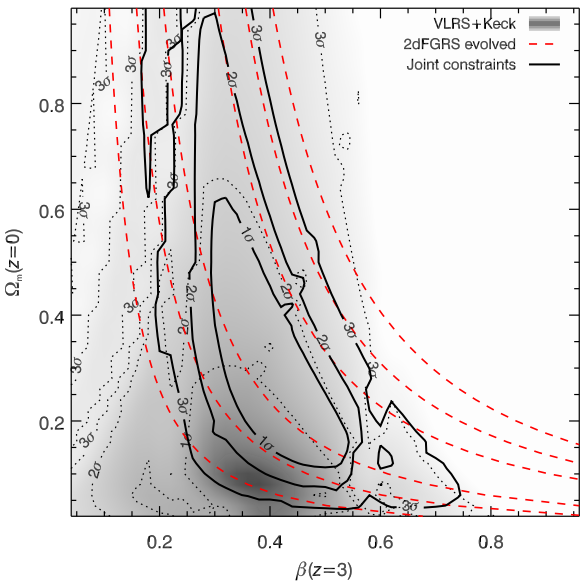

Figure 23. Fitting contours for the mass density and bulk inflow based on the combined VLRS+Keck $\xi(\sigma,\pi)$. The shaded region gives the result from the VLT+Keck data sample (assuming $\sqrt{\langle w_z^2\rangle} = 540\mathrm{kms}^{-1}$, $r_0 = 3.75\ h^{-1}\mathrm{Mpc}$ and $\gamma = 1.55$) with the dotted contour lines giving the 1, 2 and 3σ uncertainties. The results from this fit are $\beta(z=3) = 0.38^{+0.15}_{-0.13}$ and $\Omega_m(z=0) = 0.08^{+0.22}_{-0.08}$. The dashed red lines show the 1, 2 and 3σ constraints given by evolving the 2dFGRS measurements as described in the text. The solid black contours give the combination of the two and give a result of $\beta(z=3) = 0.38^{+0.16}_{-0.09}$ and $\Omega_m(z=0) = 0.30^{+0.32}_{-0.18}$.

to make more accurate measurements of both the angular and redshift survey correlation functions at these redshifts. Below the break scale is of extreme interest for single halo galaxy formation models and at large scales the interest is in looking for a flattening of the correlation function slope due to the presence of primordial non-Gaussianity.

3.5 Estimating Ω_m and the growth rate

3.5.1 The mass density of the Universe

We now look at the cosmological results afforded by the $z \approx 3$ LBG clustering and dynamics. As discussed by Hoyle et al. (2002); da Ângela et al. (2005b), it is, in principle, possible to constrain the matter density $\Omega_m(z=0)$ from the measurement of $\xi(\sigma,\pi)$. Effectively, the elongation of $\xi(\sigma,\pi)$ along the line of sight increases with increasing values of $\Omega_m(z=0)$. However, increased values of β lead to a flattening of $\xi(\sigma,\pi)$ along the line of sight. These effects combined lead to a degeneracy in determining Ω_m from the galaxy clustering alone.

In previous sections, we have studied the galaxy dynamics assuming a cosmology with $\Omega_m(z=0) = 0.3$. We now fit the $\xi(\sigma,\pi)$ result with this assumed cosmology, but now with a constant peculiar velocity of $\sqrt{\langle w_z^2\rangle} = 540\mathrm{kms}^{-1}$ and fitting for $\Omega_m(z=0)$ and β. The result is shown by the 1σ, 2σ and 3σ contours (solid) in Fig. 23. Based on just the $z=3$ galaxy clustering, we find results for the mass density of $\Omega_m(z=0) = 0.08^{+0.22}_{-0.08}$ and on the infall parameter of $\beta(z=3) = 0.38^{+0.15}_{-0.13}$.

As discussed by da Ângela et al. (2005a,b) and Paper I, by combining these results with a measurement of the amplitude of the mass clustering at low redshift, it is possible to break the degeneracy between Ω_m and β. To do this, we use the 2dFGRS measurements of Hawkins et al. (2003), who found $r_0 = 5.0\ h^{-1}\mathrm{Mpc}$, $\gamma = 1.8$ and $\beta(z=0.11) = 0.49 \pm 0.09$. We then determine the $z = 0.11$ underlying dark matter clustering amplitude from these parameter constraints and evolve this to $z=3$ for test cosmology range of $\Omega_m(z=0) = 0-1$. Finally, we estimate the bias for the LBG population from this extrapolated matter clustering amplitude and the measured LBG clustering properties we have presented in earlier sections. The constraints on β using this method over a range of assumed Ω_m values are given by the red dashed contours in Fig 23. By combining these with the original constraints from $\xi(\sigma,\pi)$, we find a result of $\beta(z=3) = 0.38^{+0.16}_{-0.09}$ and $\Omega_m(z=0) = 0.30^{+0.32}_{-0.18}$.

Across these analyses, we have consistently found a value for the infall parameter of $\beta(z=3) \approx 0.36-0.40$. Ω_m is somewhat less well constrained, but remains consistent with ΛCDM. The measurements of $\beta(z=3)$ presented here are consistent with our previous measurement from Paper I of $\beta(z=3) = 0.48 \pm 0.17$, whilst being somewhat higher than the result found by da Ângela et al. (2005a) of $\beta(z=3) = 0.15^{+0.20}_{-0.15}$. We note that the latter assumes a fixed velocity dispersion of $\sqrt{\langle w_z^2\rangle} = 400\mathrm{kms}^{-1}$ and given the degeneracy between β and $\sqrt{\langle w_z^2\rangle}$ their lower estimate of β is not surprising.

3.5.2 Growth rate results compared

In a similar fashion to the previous section, we may use the clustering and dynamics measurements to constrain the growth of structure via the growth parameter, $f(z)$. The bulk motion and the clustering bias, b, of a galaxy population are related to the growth parameter via:

$$\beta = \frac{f(z)}{b} \approx \frac{\Omega_m(z)^{0.55}}{b} \qquad (14)$$

Therefore, given measurements of the bias and dynamical infall of a range of galaxy populations across cosmic time, constraints on the growth of structure can be made. Guzzo et al. (2008) presented the results of such an analysis based on the VLT VIMOS Deep Survey (VVDS), showing values for $f(z)$ extracted from a number of galaxy surveys up to a redshift of $z \approx 0.8$. Here we add the $z \approx 3$ result from our survey. We present measurements in terms of both $f(z)$ and $f\sigma_8$, where $f\sigma_8$ is intended to give a measurement which is *less* dependent on the cosmology assumed for the calculation of the clustering (e.g. Song & Percival 2009).

We have already calculated the infall parameter and take the value ($\beta = 0.32$) obtained via fitting the velocity dispersion and β in a ΛCDM cosmology with $\Omega_m = 0.3$ and $\Omega_\Lambda = 0.7$ (Fig. 21).

The bias can be calculated directly from the clustering measurements by using the volume averaged clustering:

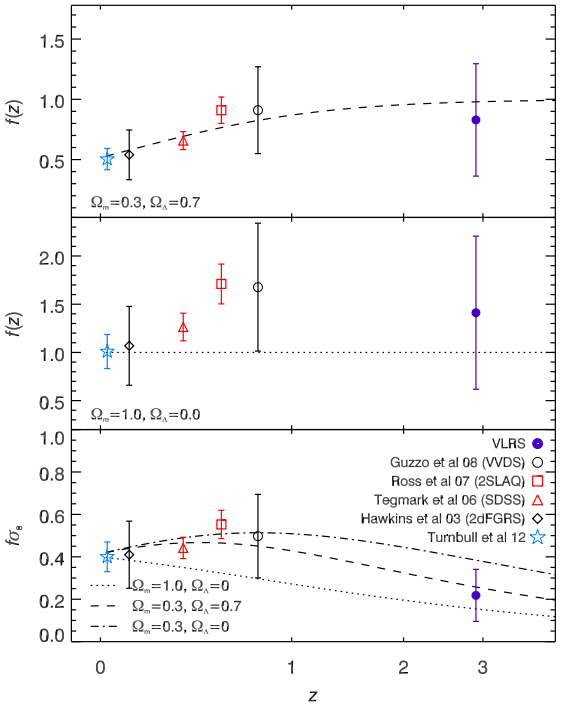

Figure 24. The evolution of the growth factor based on available $z < 1$ survey observations and the constraint from the VLRS data (solid blue circle).

$$b = \sqrt{\frac{\xi_g(s)}{\xi_{DM}(s)}} = \sqrt{\frac{\bar{\xi}_g(8)}{\bar{\xi}_{DM}(8)}} \tag{15}$$

where $\bar{\xi}_g(8)$ is the volume averaged correlation function at $s < 8\ h^{-1}$Mpc for the galaxy population and $\bar{\xi}_{DM}(8)$ is the same, but for the underlying dark matter distribution. The volume averaged clustering is calculated from the clustering using:

$$\bar{\xi}(x) = \frac{3}{x^3}\int_0^x r^2 \xi(r) \mathrm{d}r \tag{16}$$

In addition, a measure of the dark matter clustering is required in order to estimate of the bias of the galaxy population and we calculate this using the CAMB software incorporating the HALOFIT model of non-linearities (Smith et al. 2003).

Using the previously determined best fit parameters of $r_0 = 3.75\ h^{-1}$Mpc and $\gamma = 1.55$, we evaluate the galaxy bias based on a single power-law, finding a bias for the LBGs of $b = 2.59 \pm 0.11$. Combining this with our measurement of the infall parameter of $\beta = 0.32$ gives a value for the growth parameter based on the combined LBG sample of $f(z = 3) = 0.83 \pm 0.46$.

We present the $f(z = 3)$ result (filled blue circle) in the top panel of Fig. 24 alongside a number of other low-redshift measurements. In order of ascending redshift, the star shows the measurement of Turnbull et al. (2012) based on local supernovae measurements, the diamond shows the result based on the 2dFGRS presented by Hawkins et al. (2003), the red triangle shows the SDSS result based on LRGs from Tegmark et al. (2006), the red square shows the 2SLAQ result also estimated from the LRG population of Ross et al. (2007) and the black circle shows the VVDS result of Guzzo et al. (2008). For completeness these are also summarised in Table 12.

In the middle panel of Fig. 24, we also plot the evolution of $f(z)$ based on the assumed ΛCDM cosmology (dashed line), where $f(z) = \Omega_m(z)^{0.55}$. The low redshift data points are all consistent with the assumed cosmology at the $\sim 1\sigma$ level and at $z = 3$, the model cosmology is again consistent with the data. We note again that the observations themselves depend on the assumed cosmology via $\sigma_8(z)$ and so to test the $\Omega_m = 1$ cosmology we adjust the observed values of $f(z)$ for the effects of different cosmology in eq. 15 according to the methods set out by da Ângela et al. (2005a). Also assuming that β is approximately independent of the assumed cosmology, we see that the $\Omega_m = 1$ z-independent growth rate is apparently rejected by the data. However, if the bias is allowed to float rather than just fit the lowest redshift point then the model may only be rejected at the $1 - 2\sigma$ level, consistent with the conclusions from Fig. 23.

If we now consider $f\sigma_8$, the observations are now independent of the assumed cosmology, at least given again the assumption that the observed β is approximately cosmology indpendent. Each of the observational measurements is again plotted in the top panel of Fig. 24, but now in terms of $f\sigma_8$. We now plot three test cosmologies for comparison, the ΛCDM used in the top panel (dashed line), plus an Einstein-de-Sitter model ($\Omega_m = 1$, $\Omega_\Lambda = 0$, dotted line) and an open Universe without a cosmological constant and a mass density of $\Omega_m = 0.3$ (dot-dash line). For each model we incorporate a factor (c_{at}) to correct for the cosmology assumed in the measurement of the clustering observations being different from the test cosmology. Each model is thus given by:

$$(f\sigma_8)_a = \beta\sigma_{g,a} = \frac{\beta\sigma_{g,t}}{\sqrt{c_{at}}} = \frac{(f\sigma_8)_t}{\sqrt{c_{at}}} = \frac{\Omega_{m,t}(z)^{0.55}\sigma_{8,t}(z)}{\sqrt{c_{at}(z)}} \tag{17}$$

where an index of t denotes a parameter calculated in the test cosmology and an index of a denotes a parameter calculated in the assumed cosmology (i.e. ΛCDM). We normalise σ_8 to 0.8 at $z = 0$ and σ_g is effectively σ_8 measured for the galaxy population. If we assume a power-law form for the clustering with a slope of $\gamma = 1.8$, then following Ballinger et al. (1996); da Ângela et al. (2005a) c_{at} is given by:

$$c_{at} = \left(\left(\frac{B_t}{B_a}\right)^2 \frac{A_t}{A_a}\right)^{2/3} \tag{18}$$

with A and B as defined by da Ângela et al. (2005a). We are assuming here that β is independent of cosmology, a reasonable approximation when $\Omega_m \gtrsim 0.1$

With the models corrected to account for differences between the cosmology assumed for the observations and the model cosmologies, the observations now provide clearer tests on the models. We note that the observations (excepting the SDSS point) assume the $\Omega_m = 0.3/\Omega_\Lambda = 0.7$ cosmol-

Table 12. Summary of growth parameter results from the literature.

Survey	z	b	β	f	$f\sigma_8$
First Amendment SNe[1]	0.025	—	—-	—	0.40 ± 0.07
2dFGRS[2]	0.11	1.15 ± 0.06	0.47 ± 0.18	0.54 ± 0.21	0.41 ± 0.16
SDSS LRGs[3]	0.35	2.13[4]	0.31 ± 0.04	0.66 ± 0.07	0.44 ± 0.05
2SLAQ LRGs[5]	0.55	2.02 ± 0.10	0.45 ± 0.05	0.91 ± 0.11	0.55 ± 0.07
VVDS[6]	0.77	1.30 ± 0.10	0.70 ± 0.26	0.91 ± 0.07	0.50 ± 0.04
VLRS+Keck	2.90	2.59 ± 0.11	0.32 ± 0.20	0.83 ± 0.46	0.22 ± 0.12

[1] Turnbull et al. (2012) [2] Hawkins et al. (2003) [3] Tegmark et al. (2006)
[4] Song & Percival (2009) [5] Ross et al. (2007) [6] Guzzo et al. (2008)

ogy and so there is no change in the relationship between the observations and the ΛCDM model between the top and bottom panels. Thus the VLRS datapoint shows the same level of consistency with the ΛCDM model for $f\sigma_8$ and $f(z)$.

At redshifts of $z < 1$, we see that flat and open cosmologies (i.e. with and without a cosmological constant) are poorly distinguished by the available observations. At $z = 3$, we find that the VLRS data rejects the open cosmology with $\Omega_m = 0.3$ at the $\approx 2\sigma$ level. The Einstein-de Sitter cosmology is apparently rejected by combining the $z < 1$ and $z \approx 3$ observations. But again if the normalisation of the model is allowed to float rather than be fixed on the low-redshift SNe observation, the model still fits the data with a reduced χ^2 of 2.7.

4 CONCLUSIONS

We have presented the widest area spectroscopic survey of galaxies thus far in the redshift range $2 < z < 3.5$, based on observations with the VLT VIMOS instrument. This paper adds to the initial dataset of Bielby et al. (2011), where data in five $0.5^\circ \times 0.5^\circ$ fields were presented. Here we add a further four new fields, each with deep optical imaging over an area of $\approx 0.5^\circ \times 0.5^\circ$ in three cases and a full $1^\circ \times 1^\circ$ in the fourth field. In addition, we have extended one of the original fields of Paper I to $1^\circ \times 1^\circ$ from the original $0.5^\circ \times 0.5^\circ$. In total therefore, we now have ≈ 4 deg^2 of optical imaging with a minimum of three bands in each field incorporating U, B and R or equivalents.

In total, the survey now consists of 2,148 $z > 2$ galaxies. The properties of the full sample have been presented here with redshift and magnitude distributions as well as example and composite spectra. The mean redshift of our $z > 2$ galaxy dataset is $\bar{z} = 2.78$. In addition, we detect 30 AGN or quasars, ≈ 800 low-redshift galaxies and $\approx$130 Galactic stars. Using the $z > 2$ galaxy dataset, we have conducted an analysis of the galaxy clustering at $z \sim 3$. Using the semi-projected correlation function, we have measured a galaxy clustering length of $r_0 = 3.32 \pm 0.41$ h^{-1}Mpc with a slope of $\gamma = 1.53 \pm 0.26$, assuming a power-law form to $\xi(r)$. We have also combined the VLRS sample with the Keck LBG sample of Steidel et al. (2003), which provides greater statistical power on small scales (i.e. $s \lesssim 2$ h^{-1}Mpc) than the VLRS but does not provide the coverage of the VLRS at larger scales (i.e. $s \gtrsim 8$ h^{-1}Mpc). For the combined sample we measure a clustering length of $r_0 = 3.75 \pm 0.24$ h^{-1}Mpc, with a slope of $\gamma = 1.55 \pm 0.09$.

We have shown that the LBG correlation functions consistently show slopes that are significantly flatter than the canonical $\gamma = 1.8$ observed at low redshift. Indeed, the measured slopes of $\gamma = 1.55$ are flatter than in some $z \approx 1$ galaxy and radio-source correlation functions that have been interpreted as showing evidence for primordial non-Gaussianity (Xia et al. 2010; Thomas et al. 2011; Sawangwit et al. 2011; Nikoloudakis et al. In Prep). Non-Gaussianity is expected to be easier to detect at large-scales and high redshift. We have therefore checked whether a standard ΛCDM model is consistent with the form of the VLRS $\xi(s)$ in particular in the regime $10 < s < 50$ h^{-1}Mpc. We found that there is evidence that the LBGs are showing more large-scale power than the standard model in this regime but only at $\approx 2\sigma$. More studies of LBG clustering at large-scales are clearly needed to check these results.

In addition to the 1D clustering analyses, we have also investigated the 2D correlation function and the imprints of galaxy dynamics on the clustering. We find that the 2D clustering for the VLRS+Keck LBG sample is well fit by a model based on a power-law fit with a clustering length of $r_0 = 3.32$ h^{-1}Mpc, a large scale infall parameter of $\beta = 0.32 \pm 0.20$ and a velocity dispersion of $\sqrt{\langle w_z^2 \rangle} = 540^{+180}_{-200}$kms^{-1}, over a range of $1 < s < 25$ h^{-1}Mpc. We have shown that this result is consistent with the model for the redshift space correlation function, $\xi(s)$, measured for the combined sample.

Finally, we use the 2D galaxy clustering results to determine the matter density parameter and the growth parameter. Using the previously constrained form for the clustering and galaxy velocity dispersion, we fit the 2D correlation function for the matter density, Ω_m. We find an acceptable range in the matter density of $\Omega_m(z = 0) = 0.08^{+0.22}_{-0.08}$ (with an infall parameter of $\beta(z = 3) = 0.38^{+0.15}_{-0.13}$). We add a further constraint provided by the 2dFGRS low-redshift clustering measurements, which gives $\Omega_m(z = 0) = 0.30^{+0.32}_{-0.18}$ (with an infall parameter of $\beta(z = 3) = 0.38^{+0.16}_{-0.09}$). Although the constraints on the mass density are relatively weak, we see that the constraints on the infall parameter remain consistent. Using these measurements to constrain the growth parameter, we find a value of $f(z = 3) = b\beta = 0.83 \pm 0.46$. In addition we determine the combined parameter $f\sigma_8$, which gives a measure of the growth parameter that is less dependent on the assumed underlying dark matter mass distribution. In this case we find a value of $f\sigma_8 = 0.22 \pm 0.12$. These measurements are the highest redshift constraint on the growth parameter based on galaxy clustering analyses. We have shown that these measurements are consistent with the ΛCDM standard model, although given the uncertain-

ties on the measurements, they are also consistent with a number of other cosmologies.

This work is one of the largest surveys of the galaxy mass distribution at $z \approx 3$ and paves the way for a number of lines of research, which will be followed in subsequent papers. In particular, the proximity of the data presented here to quasar sightlines will provide important constraints on the relationship between galaxies and the IGM at an epoch associated with significant interactions between the two.

ACKNOWLEDGMENTS

We thank Mike Irwin for assistance with the WFCAM data reduction. This work was based on data obtained with the NOAO Mayall 4m Telescope at Kitt Peak National Observatory, USA (programme ID: 06A-0133), the NOAO Blanco 4m Telescope at Cerro Tololo Inter-American Observatory, Chile (programme IDs: 03B-0162, 04B-0022) and the ESO VLT, Paranal, Chile (programme IDs: 075.A-0683, 077.A-0612, 079.A-0442). MDH acknowledges the support of a STFC PhD Studentship grant, whilst RMB, TS and NM also acknowledge STFC funding. RMB acknowledges support from a grant obtained from the Agence Nationale de la Recherche (ANR, France). This work was partially supported by the Consejo Nacional de Investigaciones Científicas y Tćnicas and Secretaria de Ciencia y Tćnica de la Universidad Nacional de Córdoba, and the European Union Alfa II Programme, through LENAC, the Latin American-European Network for Astrophysics and Cosmology. DM and LI are supported by FONDAP CFA 15010003, and BASAL CATA PFB-06. This research has made use of the NASA/IPAC Extragalactic Database (NED) which is operated by the Jet Propulsion Laboratory, California Institute of Technology, under contract with NASA.

REFERENCES

Adelberger K. L., Shapley A. E., Steidel C. C., Pettini M., Erb D. K., Reddy N. A.,. 2005a, ApJ, 629, 636
Adelberger K. L., Steidel C. C., Pettini M., Shapley A. E., Reddy N. A., Erb D. K.,. 2005b, ApJ, 619, 697
Adelberger K. L., Steidel C. C., Shapley A. E., Pettini M.,. 2003, ApJ, 584, 45
Ballinger W. E., Peacock J. A., Heavens A. F.,. 1996, MNRAS, 282, 877
Baugh C. M., Gardner J. P., Frenk C. S., Sharples R. M.,. 1996, MNRAS, 283, L15
Bertin E., Mellier Y., Radovich M., Missonnier G., Didelon P., Morin B.,. 2002, in Astronomical Society of the Pacific Conference Series, Vol. 281, Astronomical Data Analysis Software and Systems XI, ed. D. A. Bohlender, D. Durand,,T. H. Handley, 228–+
Bielby R., Shanks T., Sawangwit U., Croom S. M., Ross N. P., Wake D. A.,. 2010, MNRAS, 403, 1261
Bielby R. M., et al. . 2011, MNRAS, 414, 2
Blake C., et al. . 2009, MNRAS, 395, 240
Bolzonella M., Miralles J., Pelló R.,. 2000, A&A, 363, 476
Chapman S. C., Blain A. W., Smail I., Ivison R. J.,. 2005, ApJ, 622, 772
Constantin A., Shields J. C., Hamann F., Foltz C. B., Chaffee F. H.,. 2002, ApJ, 565, 50
Cooke J., Wolfe A. M., Gawiser E., Prochaska J. X.,. 2006, ApJ, 652, 994
Cowie L. L., Hu E. M.,. 1998, AJ, 115, 1319
Crain R. A., et al. . 2009, MNRAS, 399, 1773
Crighton N. H. M., et al. . 2011, MNRAS, 414, 28
da Ângela J., Outram P. J., Shanks T.,. 2005a, MNRAS, 361, 879
da Ângela J., Outram P. J., Shanks T., Boyle B. J., Croom S. M., Loaring N. S., Miller L., Smith R. J.,. 2005b, MNRAS, 360, 1040
Fine S., Croom S. M., Bland-Hawthorn J., Pimbblet K. A., Ross N. P., Schneider D. P., Shanks T.,. 2010, MNRAS, 409, 591
Foucaud S., McCracken H. J., Le Fèvre O., Arnouts S., Brodwin M., Lilly S. J., Crampton D., Mellier Y.,. 2003, A&A, 409, 835
Franx M., et al. . 2003, ApJ, 587, L79
Gawiser E., et al. . 2007, ApJ, 671, 278
Gawiser E., et al. . 2006, ApJ, 642, L13
Giavalisco M., Dickinson M.,. 2001, ApJ, 550, 177
Groth E. J., Peebles P. J. E.,. 1977, ApJ, 217, 385
Guzzo L., et al. . 2008, Nature, 451, 541
Hawkins E., et al. . 2003, MNRAS, 346, 78
Hildebrandt H., et al. . 2012, MNRAS, 2386
Hildebrandt H., Pielorz J., Erben T., Schneider P., Eifler T., Simon P., Dietrich J. P.,. 2007, A&A, 462, 865
Hildebrandt H., Pielorz J., Erben T., van Waerbeke L., Simon P., Capak P.,. 2009, A&A, 498, 725
Hoyle F., Outram P. J., Shanks T., Boyle B. J., Croom S. M., Smith R. J.,. 2002, MNRAS, 332, 311
Ivison R. J., et al. . 2002, MNRAS, 337, 1
Jenkins A., et al. . 1998, ApJ, 499, 20
Kim H., Baugh C. M., Cole S., Frenk C. S., Benson A. J.,. 2009, MNRAS, 400, 1527
Le Fèvre O., et al. . 2003, in Society of Photo-Optical Instrumentation Engineers (SPIE) Conference Series, Vol. 4841, Society of Photo-Optical Instrumentation Engineers (SPIE) Conference Series, ed. M. Iye & A. F. M. Moorwood, 1670–1681
Lowenthal J. D., et al. . 1997, ApJ, 481, 673
Madau P., Ferguson H. C., Dickinson M. E., Giavalisco M., Steidel C. C., Fruchter A.,. 1996, MNRAS, 283, 1388
Magdis G. E., et al. . 2010, MNRAS, 409, 22
Massey R., et al. . 2007, Nature, 445, 286
McCracken H. J., Le Fèvre O., Brodwin M., Foucaud S., Lilly S. J., Crampton D., Mellier Y.,. 2001, A&A, 376, 756
Mo H. J., White S. D. M.,. 1996, MNRAS, 282, 347
Nikoloudakis N., Shanks T., Sawangwit U.,. In Prep
Norberg P., et al. . 2002, MNRAS, 332, 827
Orsi A., Lacey C. G., Baugh C. M., Infante L.,. 2008, MNRAS, 391, 1589
Ouchi M., et al. . 2005, ApJ, 635, L117
Ouchi M., et al. . 2008, ApJS, 176, 301
Peebles P. J. E.,. 1980, "The Large-Scale Structure of the Universe" (Princeton University Press)
Pettini M., Shapley A. E., Steidel C. C., Cuby J.-G., Dickinson M., Moorwood A. F. M., Adelberger K. L., Giavalisco M.,. 2001, ApJ, 554, 981
Phleps S., Peacock J. A., Meisenheimer K., Wolf C.,. 2006, A&A, 457, 145

Rakic O., Schaye J., Steidel C. C., Rudie G. C.,. 2011, MNRAS, 414, 3265
Roche N., Shanks T., Metcalfe N., Fong R.,. 1993, MNRAS, 263, 360
Ross N. P., et al. . 2007, MNRAS, 381, 573
Sawangwit U., Shanks T., Abdalla F. B., Cannon R. D., Croom S. M., Edge A. C., Ross N. P., Wake D. A.,. 2011, MNRAS, 416, 3033
Shanks T., Bielby R., Infante L.,. 2011, The Messenger, 143, 42
Shapley A. E., Steidel C. C., Pettini M., Adelberger K. L.,. 2003, ApJ, 588, 65
Smail I., Ivison R. J., Blain A. W., Kneib J.,. 2002, MNRAS, 331, 495
Smith R. E., et al. . 2003, MNRAS, 341, 1311
Song Y.-S., Percival W. J.,. 2009, J. Cosmology Astropart. Phys., 10, 4
Springel V., Frenk C. S., White S. D. M.,. 2006, Nature, 440, 1137
Springel V., et al. . 2005, Nature, 435, 629
Steidel C. C., Adelberger K. L., Giavalisco M., Dickinson M., Pettini M.,. 1999, ApJ, 519, 1
Steidel C. C., Adelberger K. L., Shapley A. E., Pettini M., Dickinson M., Giavalisco M.,. 2003, ApJ, 592, 728
Steidel C. C., Erb D. K., Shapley A. E., Pettini M., Reddy N., Bogosavljević M., Rudie G. C., Rakic O.,. 2010, ApJ, 717, 289
Steidel C. C., Giavalisco M., Pettini M., Dickinson M., Adelberger K. L.,. 1996, ApJ, 462, L17+
Tegmark M., et al. . 2006, Phys. Rev. D, 74, 123507
Thomas S. A., Abdalla F. B., Lahav O.,. 2011, Physical Review Letters, 106, 241301
Turnbull S. J., Hudson M. J., Feldman H. A., Hicken M., Kirshner R. P., Watkins R.,. 2012, MNRAS, 420, 447
Xia J.-Q., Viel M., Baccigalupi C., De Zotti G., Matarrese S., Verde L.,. 2010, ApJ, 717, L17